Computers and Geotechnics 156 (2023) 105306

Contents lists available at ScienceDirect

Computers and Geotechnics

journal homepage: www.elsevier.com/locate/compgeo

Research Paper

Influence of static–cyclic load misalignment on the drained tilting response of offshore monopiles in sand

Zheng Li [a], Haoyuan Liu [b], Michael A. Hicks [a], Federico Pisanò [a,*]

[a] Geo-Engineering Section, Faculty of Civil Engineering and Geosciences, Delft University of Technology, Delft, Netherlands
[b] Advanced Modelling Section, Norwegian Geotechnical Institute, Oslo, Norway

ARTICLE INFO

Keywords:
Finite-element modelling
Footings/foundations
Load misalignment
Offshore engineering
Cyclic loading
Sand

ABSTRACT

Offshore monopile foundations are exposed to misaligned wind and wave loadings, which are respectively dominated by (nearly) static and cyclic load components. While the response of these systems to unidirectional cyclic loading has been extensively investigated, only a few studies have been devoted to the realistic case of misaligned static and cyclic loads, and particularly to the effects of such misalignment on the accumulation of pile rotation under prolonged cycling. This paper presents a 3D finite-element (FE) modelling study on the relationship between load misalignment and cyclic monopile tilt under drained conditions, based on the use of the SANISAND-MS model to enable accurate simulation of cyclic sand ratcheting. After qualitatively identifying the relationship between relevant loading parameters and cyclic stress/densification mechanisms in the soil, specific parametric studies are performed to explore the impact on pile tilt accumulation. The results show that, in comparison to unidirectional loading, misaligned static–cyclic loading gives rise to lesser-known pile–soil interaction mechanisms: when the direction of cycling deviates from that of the static load, "cyclic compression" and "direct cyclic shearing" mechanisms begin to co-exist. This is quantitatively captured by a newly proposed empirical equation for monopile tilt calibrated against the 3D FE simulation results obtained in this work.

1. Introduction

The offshore wind sector has been decisively accelerating, especially in Europe, over the last decade, with an increase of the yearly average size of offshore wind turbines (OWTs) from 3 MW in 2010 to 8.2 MW in 2020 and likely to reach 10~13 MW within the next OWT generation (Ramírez et al., 2020). These remarkable offshore structures must be designed to withstand ever harsher environmental conditions, including wind and wave loads characterised by continuous variation in amplitude, direction, and dominant frequency. Since OWTs are expected to withstand around 10^8 loading cycles during their lifetime (Achmus et al., 2009), it is important to guarantee full serviceability of the support structure and, in particular, to prevent the accumulation of an overall permanent rotation larger than 0.5° (DNV, 2016). Such a strict requirement renders the design of OWT foundations quite challenging, especially in light of the conceptual and computational complexity that long-term soil–structure deformation analyses still entail (Pisanò, 2019). To date, steel tubular monopiles continue to be the preferred foundation solution for OWTs, owing to their cost-effectiveness and suitability for mass-production. While offshore pile design methodologies for the oil and gas industry have been originally developed with an emphasis on capacity requirements (API, 2011; Kaynia, 2021), OWT monopile design requires a different focus on serviceability, structural fatigue, and dynamic response features (Arany et al., 2017; Byrne et al., 2019). In this context, predicting the cyclic accumulation of monopile rotation (tilt) and the associated variations in lateral stiffness has become a subject of utmost importance.

So far, empirical methods based on simple power-law equations have been widely used to describe the lateral tilt of piles under repeated loading cycles of constant amplitude (LeBlanc et al., 2010a; Klinkvort and Hededal, 2013; Frick and Achmus, 2020). Most commonly, the accumulation of pile tilt is expressed as a function of the permanent rotation after one cycle, the characteristics of the input cyclic loading, and the number n of elapsed cycles — the formulation of a direct dependence on n is also commonly referred to as an *explicit* cyclic analysis approach (Niemunis et al., 2005). An extension of this empirical approach to the case of multi-amplitude cyclic loading sequences has been proposed by resorting to so-called Miner's rule (Lin and Liao, 1999; Li et al., 2015; Truong et al., 2019) in combination with the *rainflow counting method* (Kaggwa et al., 1991), which enables the conversion of an irregular loading history into a sequence

* Corresponding author.
E-mail address: F.Pisano@tudelft.nl (F. Pisanò).

https://doi.org/10.1016/j.compgeo.2023.105306
Received 6 June 2022; Received in revised form 2 December 2022; Accepted 28 January 2023

of multiple load packages of individually constant cyclic amplitude. Although rainflow-counting analyses may lead to disregarding certain loading history effects (Leblanc et al., 2010b; Page et al., 2021), the mentioned empirical approach seems to be reasonably well-suited to support geotechnical designers in practical cyclic pile tilt calculations. On the other hand, most of the available research focuses on the case of one-directional cyclic loading, while in reality wind and wave loads may come from different directions at the same time and change significantly in intensity and direction (Rudolph et al., 2014). Nevertheless, the limited research conducted so far on the multi-directional cyclic response of monopiles has produced a number of interesting findings:

(a) when cyclic loading is applied orthogonally to the direction of a (nearly) static load component, cyclic monopile tilt tends to accumulate predominantly along the direction of the latter — see, e.g., the recent studies by Sheil and McCabe (2017) and Richards et al. (2020);
(b) the presence of misaligned static and cyclic load components can possibly give rise to larger monopile tilt accumulation than in the case of fully one-directional loading — as found, for instance, by Dührkop and Grabe (2008), Rudolph et al. (2014), Nanda et al. (2017), and Richards et al. (2020) in the presence of *fan-type*, multi-directional cyclic loading. Furthermore, asymmetric cyclic loading applied with an inclination with respect to a static load has also been found to be more 'damaging' from a monopile rotation standpoint (Jenck et al., 2021);
(c) misalignment between loading and displacement directions. In this respect, Peralta (2010) experimentally applied a closed, square load path on the head of a test pile, and found that the corresponding displacement response was instead characterised by an approximately rectangular, though not closed, path.

The study by Zhu et al. (2018) on short suction caissons provided evidence that a change in the direction of cyclic loading can lead to different rotation responses depending on whether such a change is applied at once or in gradual steps. This finding might be due to the fact that the soil state (e.g., in terms of stress field and relative density) after lateral loading is non-uniform around the monopile and therefore, as the loading direction is varied, the foundation tends to engage portions of soil that are characterised by different current states, which gives rise to quantitatively different deformations. Generally, the multi-directionality of the lateral loads has been found to have little influence on the natural frequency of monopile-supported OWTs (Lovera et al., 2019), as well as on the uniaxial ultimate capacity of the foundation (Zhu et al., 2018; Zhao et al., 2020).

In parallel to describing the mechanical behaviour of monopiles under multi-directional cyclic loading, a few authors have also begun to develop engineering modelling approaches for the numerical simulation of multi-directional monopile responses, for instance by resorting to either distributed/$p-y$ (Lovera et al., 2021) or lumped/macroelement (Page et al., 2019) models.

This paper focuses on the drained cyclic behaviour of monopiles subjected to cyclic loading in which the constant/static and variable/cyclic components are misaligned. In order to gain insight into relevant features of the behaviour, 3D FE modelling is adopted in combination with the cyclic SANISAND-MS model (Liu et al., 2019), which is well-suited to reproduce the ratcheting behaviour of sandy soils under prolonged cycling. Following recent 3D FE work on the one-directional cyclic response of monopiles (Pisanò, 2019; Liu et al., 2022a), the capabilities of the SANISAND-MS model are exploited herein to highlight relevant links between local soil behaviour and global monopile response (Cheng et al., 2021). To this end, the results of extensive parametric studies are presented, including variations in the static load magnitude, the amplitude and asymmetry of the cyclic load component, and the degree of misalignment between the two load components. Finally, the whole set of 3D FE results are exploited to feed into a new extension of the empirical method by LeBlanc et al. (2010a) for the case of misaligned static–cyclic loads.

2. 3D FE modelling of cyclic monopile–soil interaction

2.1. 3D FE model and SANISAND-MS model parameters

All the numerical simulation results presented in this paper were obtained using a 3D FE model largely based on the development/validation work of Liu et al. (2022a) – the main differences are exclusively related to the assumed lateral loading conditions, either one-directional (Liu et al., 2022a) or with static–cyclic misalignment (this study). Cyclic monopile–soil interaction analyses were carried out using the 3D FE modelling capabilities available in OpenSees (sequential version) (McKenna, 2011), which have been previously enhanced with an implementation of the SANISAND-MS model (Liu et al., 2022a) built on the existing SANISAND2004 code developed at the University of Washington (Ghofrani and Arduino, 2018).

Fig. 1 shows the 3D FE model adopted in this study. As in Liu et al. (2022a), the FE model features a steel monopile (founded in sand) of diameter $D = 5$ m, embedded length $L = 20$ m, and wall thickness $t = 0.1$ m, with elastic properties equal to $E = 220$ GPa (Young's modulus) and $\nu = 0.3$ (Poisson's ratio). While the soil domain and embedded portion of the monopile were discretised using 8-node stabilised single-point (SSP) brick elements (McGann et al., 2015), the pile above the soil surface was modelled as a Timoshenko beam of equivalent bending stiffness. Such a beam facilitated the application of external lateral loads with an eccentricity $e = L$ with respect to the mudline.

Regarding the modelling of the sand's cyclic behaviour, the earliest version of the SANISAND-MS model was adopted to enable realistic simulation of cyclic ratcheting behaviour (Liu et al., 2019; Liu and Pisanò, 2019), owing to the enhancement of the original SANISAND bounding surface model (Dafalias and Manzari, 2004) with an additional memory locus (Corti et al., 2016). The proven good performance of the model under non-standard triaxial loading conditions (Liu et al., 2019), in which independent cyclic variations of both axial and radial stress give rise to a more complex, polarised stress path in the $q-p$ plane, is relevant for the present study. As is shown in Fig. 2, SANISAND-MS can capture the effect of the stress path polarisation angle on the cyclic ratcheting response. Furthermore, the model – both in its first and upgraded (Liu et al., 2018, 2020) versions – has been successfully applied to the 3D FE analysis of offshore monopiles under lateral cyclic loading, and has shown encouraging performance with respect to the simulation of pile tilt accumulation under different loading and drainage conditions (Liu et al., 2022a; Cheng et al., 2021; Liu and Kaynia, 2021; Liu et al., 2022b).

Given the focus of this study on low-frequency cyclic loading in (permeable) sandy soil, inertial and hydro-mechanical coupling effects were disregarded, so that all cyclic simulations were performed in dry sand (fully drained conditions) using the OpenSees' quasi-static FE solver. The reference soil parameters calibrated by Liu et al. (2019) for Karlsruhe quartz sand (Wichtmann, 2005) were adopted in all cases as reported in Table 1 – the specific gravity G_s of the soil particles equals 2.6, while the dry unit weight γ_{dry} may be obtained for any relative density based on the known values of the maximum (e_{max}=0.874) and minimum (e_{min}=0.577) void ratios. The interface between the monopile and the soil was modelled as a thin layer of soil (of thickness equal to $0.01D$) of reduced critical stress ratio (M_c) and dimensionless shear stiffness (G_0) (both 2/3 of the corresponding intact soil's properties), following the simplified approach by Griffiths (1985) (see also Corciulo et al., 2017; Kementzetzidis et al., 2019 for recent application to monopile 3D FE modelling).

Overall, the 3D FE model in Fig. 1 is in all respects similar to the model set up and verified by Liu et al. (2022a). In summary:

– boundary conditions were imposed on the soil domain to obtain a fully fixed bottom surface, a free upper surface, and no horizontal displacement along the direction perpendicular to the lateral surface;

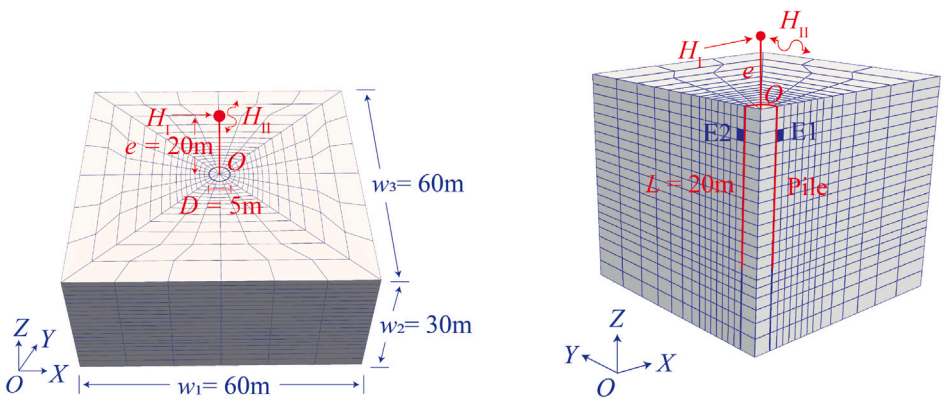

(a) Full model (b) One-quarter of the full model

Fig. 1. Space discretisation of the 3D monopile–soil model.

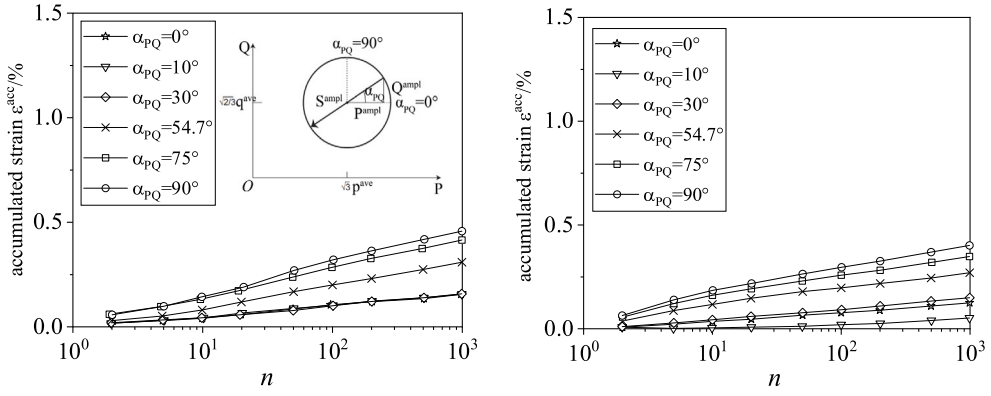

(a) Experimental data(Wichtmann, 2005) (b) Model simulation(Liu et al., 2019)

Fig. 2. (a) Cyclic triaxial test results with imposed stress path polarisation and (b) corresponding SANISAND-MS simulation — redrawn after (Liu et al., 2019).

Table 1
Karlsruhe sand SANISAND-MS model parameters — after Liu et al. (2019).

Elasticity		Critical state					Yield surface	Plastic modulus			Dilatancy		Memory surface		
G_0	ν	M_c	c	λ_c	e_0	ξ	m	h_0	c_h	n^b	A_0	n^d	μ_0	ζ	β
110	0.05	1.27	0.712	0.049	0.845	0.27	0.01	5.95	1.01	2.0	1.06	1.17	260	0.0005	1

– both the soil and the embedded monopile were discretised using the 8-node brick elements of the stabilised, single-point (SSP) type proposed by McGann et al. (2015);
– non-linear static simulations were performed with implicit time integration and each step solved iteratively using the Krylov–Newton algorithm described by Scott and Fenves (2003);
– SANISAND-MS constitutive equations were integrated in time using an explicit, fourth-order Runge–Kutta algorithm, featuring automatic error control and sub-stepping (Sloan, 1987; Liu et al., 2022a).

Since this work deals with misaligned static and cyclic load components, however, it was not possible to exploit any geometrical symmetries of the system to reduce computational costs — nevertheless, it was verified that the complete 3D model in Fig. 1 returns, under unidirectional lateral loading, the same results that one would obtain using Liu et al.'s reduced half model.

2.2. Load application and monopile tilt: relevant definitions

It is well-known that OWTs are subjected to wind and wave loads that may act along different spatial directions. In order to study the effects of multi-directional cyclic loading on the lateral response of monopiles, small-scale experimental studies have been recently performed, e.g., regarding the application of T- and L-shaped loading paths (Figs. 3(c)–3(d)) to investigate unexplored load misalignment effects (Richards, 2019; Richards et al., 2020, 2021). In this respect, the combination of static and cyclic load components is typically regarded as an idealised representation of, respectively, slow/nearly-steady wind loading and substantially variable (cyclic) wave loading.

As illustrated in Fig. 3(a), this numerical study considers loading scenarios (of pile moment M at the mudline) in which, with respect to an arbitrary system of orthogonal coordinates X and Y, the static load M_{stat} is applied at an angle Φ with respect to the X direction, while an angle γ defines the misalignment between the static and cyclic loading directions (directions I and II, respectively). These loads intersect at a point O'; since regular cyclic loading can always be described as the combination of an average (M_{av}) and a cyclic/variable (M_{cyc}) component, the distance along II between O' and M_{av} directly quantifies the asymmetry of the cycling with respect to M_{stat} – in this context, M_{av} coinciding with O' will determine a case of symmetric cyclic loading. For simplicity (and with no loss of generality for a uniform soil deposit), M_{stat} will henceforth be assumed to act along the X direction (i.e., $\Phi = 0°$); while the case $\gamma = 0°$ identifies aligned

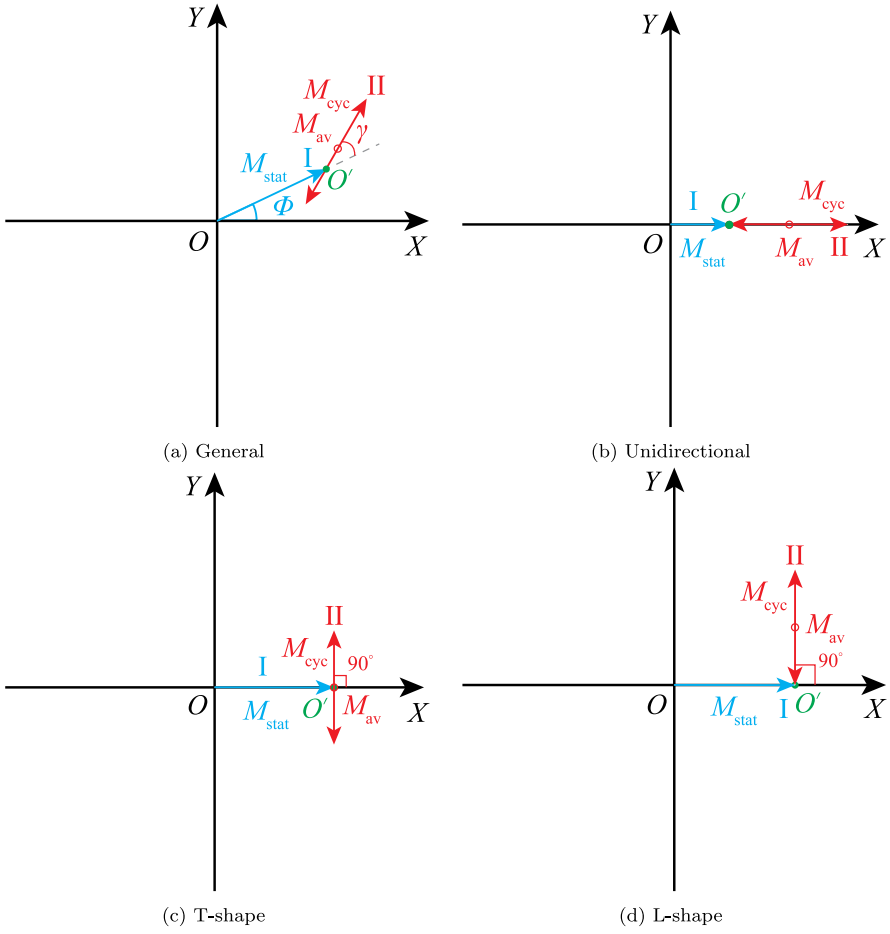

Fig. 3. Schematic representation of misaligned static and cyclic loads, including the special cases of unidirectional (aligned) and T-/L-shaped loading.

static and cyclic loads (unidirectional loading, Fig. 3(b)), $\gamma = 90°$ can be associated with either T-shape (Fig. 3(c)) or L-shape (Fig. 3(d)) loading, depending on whether the cycling is symmetric or asymmetric with respect to M_{stat}. All 3D FE simulations were performed according to the following three-stage pile loading procedure: (1) application of the static base-load M_{stat}; (2) load re-orientation (according to the misalignment angle γ and further loading up to the established cyclic average load M_{av}; (3) application of sinusoidal cycling M_{cyc} around M_{av}.

With reference to simplest unidirectional loading conditions, LeBlanc et al. (2010a) introduced two dimensionless load factors, ζ_b and ζ_c, to describe the main features of single-amplitude cyclic loading programmes: $\zeta_b = M_{max}/M_R$ quantifies the relative magnitude of the cyclic load component and $\zeta_c = M_{min}/M_{max}$ its asymmetry. In these definitions, M_{max} and M_{min} denote the maximum and the minimum values of the applied moment load (at the mudline), respectively, whereas the reference load M_R is usually associated with the lateral capacity of the pile at hand — henceforth conventionally associated with a rigid rotation θ_R of 2° under monotonic lateral loading. For the monopile considered herein, M_R equals to 26 800 kN and 15 450 kN in dense and loose sand, respectively — as previously reported by Liu et al. (2022a). Building on this set of definitions, LeBlanc et al. (2010a) proposed the following empirical law to describe the cyclic accumulation of monopile rotation under unidirectional/single-amplitude cyclic loading:

$$\frac{\Delta\theta}{\theta_R} = T_b(\zeta_b, D_r)\cdot T_c(\zeta_c)\cdot n^{\alpha} \tag{1}$$

where T_b (depending on ζ_b and the relative density D_r) and T_c (depending on ζ_c) are two functions that express the influence of the external loading conditions – T_b and T_c are assumed to be unrelated, with the working assumption that $T_c = 1$ when $\zeta_c = 0$. The exponent α quantifies the dependence of the normalised pile rotation on the number n of elapsed loading cycles — it should be noted that $\Delta\theta$ is normalised with respect to θ_R following Richards (2019), which is slightly, though insubstantially, different from the original normalisation proposed by LeBlanc et al. (2010a). Several studies have already confirmed that the largest tilting rate is achieved for a ζ_c value between −1 and 0, i.e., under biased two-way loading conditions (Klinkvort and Hededal, 2013; Albiker et al., 2017; Frick and Achmus, 2020; Liu et al., 2022a).

In order to extend to the case of misaligned static–cyclic loads, the above definitions of ζ_b and ζ_c were extended by considering the two different loading directions, I (static) and II (cyclic) – see Fig. 3(a) and Eqs. (2)–(5):

$$\zeta_{b,I} = \frac{M_{max,I}}{M_R}, \quad \zeta_{c,I} = \frac{M_{min,I}}{M_{max,I}} = 1 \tag{2}$$

$$\zeta_{b,II} = \frac{M_{max,II}}{M_R}, \quad \zeta_{c,II} = \frac{M_{min,II}}{M_{max,II}} \tag{3}$$

$$\zeta_{av} = \frac{M_{av}}{M_R} = \frac{(M_{max,II} + M_{min,II})/2}{M_R} = \frac{\zeta_{b,II}\,(1+\zeta_{c,II})}{2} \tag{4}$$

$$\zeta_{cyc} = \frac{M_{cyc}}{M_R} = \frac{(M_{max,II} - M_{min,II})/2}{M_R} = \frac{\zeta_{b,II}\,(1-\zeta_{c,II})}{2} \tag{5}$$

It is worth noting that, while $\zeta_{c,I}$ is necessarily always equal to 1 for the static load component, ζ_{av} and ζ_{cyc} denote the normalised cyclic mean load and amplitude — obtained by using a value of M_R that is assumed to be independent of the loading direction (which holds true for a uniform soil deposit). It is also important to acknowledge that, if

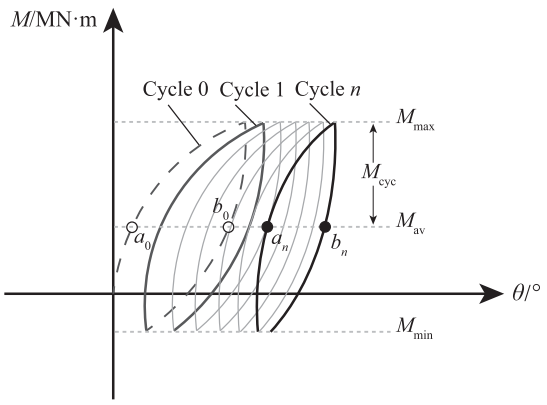

Fig. 4. Schematic moment–rotation response of a monopile subjected to cyclic loading.

the direction of a second loading is different with respect to the first loading, the path of the pile deflection may generally deviate from the direction of the second loading; therefore the X and Y components of the pile deflection (or rotation) need to be explicitly specified for clarity.

Fig. 4 shows a schematic representation of the cyclic moment–rotation response of a monopile. Following the same definitions introduced by Richards et al. (2020), the total mean rotation at the nth cycle is defined as

$$\theta_n = \frac{1}{2}(\theta_{a_n} + \theta_{b_n}) \tag{6}$$

where the subscripts a and b refer, respectively, to the loading and unloading branches within the considered cycle. Therefore, the accumulated mean rotation at the nth cycle is equal to

$$\Delta\theta_n = \theta_n - \theta_0 \tag{7}$$

The definitions in Eqs. (6)–(7) will be used to describe the pile rotation (in degrees) along both the X and Y axes.

2.3. Numerical simulation programme

This paper aims to shed new light on the influence of static–cyclic load misalignment on the tilting response of laterally loaded monopiles, with emphasis on the role played by relevant loading factors. To this end, 3D FE SANISAND-MS parametric studies were performed for the cases of T-/L-shaped and unidirectional loading, for different values of the soil relative density ($D_r = 70, 30\%$) and of the loading factors defined in Eqs. (2)–(5). The complete lists of simulations performed for each loading type are reported in Tables 2–4, along with the respective relevant specifications. In addition to the definitions in Eqs. (2)–(5), Table 4 also reports the values of two further loading factors:

$$\zeta_{b,u} = \zeta_{b,I} + \zeta_{b,II} \tag{8}$$

$$\zeta_{c,u} = \frac{\zeta_{b,I}\zeta_{c,I} + \zeta_{b,II}\zeta_{c,II}}{\zeta_{b,u}} \tag{9}$$

where $\zeta_{b,u}$ and $\zeta_{c,u}$ are only meaningful for unidirectional cycling (hence the subscript u) and are completely equivalent to the factors ζ_b and ζ_c used in Eq. (1) (LeBlanc et al., 2010a). Nevertheless, the associated values of $\zeta_{b,I-II}$, $\zeta_{c,I-II}$, ζ_{av}, ζ_{cyc} are also reported in Table 4 to enable direct comparison to the values in Tables 2–3.

All simulations were performed on a standard workstation equipped with one Xeon processor (4 cores) of 3.6 GHz, which led to a calculation time of $2 \sim 3$ weeks for the analysis of 100 load cycles in combination with the discrete 3D FE model in Fig. 1. Given the high computational effort, it would be impractical to consider many more loading cycles; however, the results presented below provide novel information, based on state-of-the-art cyclic modelling, regarding the relevant geotechnical mechanisms. In the future, it will be possible to translate this information into more efficient engineering models, either 0D or 1D.

3. Pile response to misaligned static–cyclic loading

3.1. General features of cyclic pile behaviour

Fig. 5 gives a general impression of the simulated tilting response of a monopile subjected to T- and L-shaped loading, with either orthogonal ($\gamma = 90°$, T and L labels in the figure legends) or non-orthogonal ($\gamma \neq 90°$, TV and LV labels in the figure legends) static–cyclic misalignment, both in dense ($D_r = 70\%$) and loose ($D_r = 30\%$) sand. In all considered cases, it is seen that the lateral tilting rate of the monopile tends to decrease with the number of cycles along any relevant spatial direction, which is in line with the type of cyclic ratcheting behaviour reproduced by the adopted SANISAND-MS model (Liu et al., 2019).

Figs. 5(a) and 5(b) show that the (normalised) rotational response of the pile along the two spatial directions, X and Y, is mostly along the X direction (the direction of the static load) under orthogonal T-shaped cyclic loading (cases T2 and T11, i.e., regardless of the sand density), whereas the asymmetry associated with L-shaped loading (cases L5 and L15, with $\zeta_{c,II} > -1$) leads to comparable rotation accumulation along both the X and Y directions. These phenomenon are qualitatively in good agreement with the experimental findings of Richards et al. (2020). Besides, the asymmetry of L-shaped loading seems to enhance the pile tilt along the direction X of the static load. At the same time, T2 and L5 (and also loose sand cases, T11 and L15) feature the same cyclic load amplitude ζ_{cyc} and indeed exhibit almost identical cyclic rotation excursions when the 100th cycle is approached.

Figs. 5(c) and 5(d) exemplify the tilting response of the pile under non-orthogonal T- and L-shaped loading, in dense and loose sand, respectively; in dense sand, a load misalignment angle of $\gamma = 30°$ is considered (cases TV8 and LV8), while two examples for $\gamma = 60°$ are illustrated for the reference pile in loose sand (cases TV18 and LV18). In these plots, a green line is used to connect the middle points in each cycle of the considered pile rotation path. It is seen that, while the load and pile rotation directions are substantially different at the onset of cycling, they eventually tend to align as the number of loading cycles increases — with a practically perfect match achieved within the 100 cycles considered herein. At the same time, it is also worth noting that the rotation path in dense sand under non-orthogonal T-shaped loading (TV8 case) eventually becomes symmetric about the X axis, while the same phenomenon does not occur for the same pile in loose sand. Furthermore, the non-orthogonal T-shaped loading cases, TV8 and TV18, appear to produce larger pile tilt along the X direction than their orthogonal T-shaped loading counterparts, cases T2 and T11.

An additional comparison to the unidirectional response is provided in Figs. 5(e) and 5(f). Specifically, the L-shaped loading cases, L5 and L15, are compared in terms of moment–rotation response along the Y direction to the unidirectional cases, U3 and U8, characterised by the same cyclic loading features (amplitude and asymmetry). It is clear that the presence of an initial static preload has a substantial impact on the initial stiffness (under the initial static loading ramp) and the gradual tilt accumulation — especially in loose sand. On the other hand, the same figures (top-left corner) show that, after simple translation along the θ_Y axis, the shape of the response cycles (particularly their loop area) is almost insensitive to the presence of M_{stat} and the cycling orientation — see the almost overlapping 1st, 10th, 100th cycles associated with L-shaped (dashed red lines) and unidirectional (solid black lines) loading. This finding is, for instance, relevant to assessing whether the cyclic pile–soil damping may or may not be affected by load misalignment effects, which seems not to be the case based on the 3D FE results obtained in this study.

Table 2
Numerical simulation programme for T-shaped loading cases.

Simulation label	Relative density D_r/%	Misalignment angle γ/°	ζ_b		ζ_c		ζ_{av}	ζ_{cyc}
			I	II	I	II		
T1	70	90	0.1	0.1	1	−1	0	0.1
T2	70	90	0.2	0.1	1	−1	0	0.1
T3	70	90	0.3	0.1	1	−1	0	0.1
T4	70	90	0.2	0.05	1	−1	0	0.05
T5	70	90	0.2	0.15	1	−1	0	0.15
T6	70	90	0.2	0.175	1	−1	0	0.175
T7	70	90	0.2	0.2	1	−1	0	0.2
TV8	70	30	0.2	0.1	1	−1	0	0.1
TV9	70	60	0.2	0.1	1	−1	0	0.1
T10	30	90	0.1	0.1	1	−1	0	0.1
T11	30	90	0.2	0.1	1	−1	0	0.1
T12	30	90	0.3	0.1	1	−1	0	0.1
T13	30	90	0.2	0.05	1	−1	0	0.05
T14	30	90	0.2	0.15	1	−1	0	0.15
T15	30	90	0.2	0.175	1	−1	0	0.175
T16	30	90	0.2	0.2	1	−1	0	0.2
TV17	30	30	0.2	0.1	1	−1	0	0.1
TV18	30	60	0.2	0.1	1	−1	0	0.1

Note: The label T stands for T-shaped loading with $\gamma = 90°$, while TV stands for $\gamma \neq 90°$ (non-orthogonal static and cyclic load directions).

Table 3
Numerical simulation programme for L-shaped loading cases.

Simulation label	Relative density D_r/%	Misalignment angle γ/°	ζ_b		ζ_c		ζ_{av}	ζ_{cyc}
			I	II	I	II		
L1	70	90	0.1	0.1	1	0	0.05	0.05
L2	70	90	0.2	0.1	1	0	0.05	0.05
L3	70	90	0.3	0.1	1	0	0.05	0.05
L4	70	90	0.2	0.2	1	−0.5	0.05	0.15
L5	70	90	0.2	0.2	1	0	0.1	0.1
L6	70	90	0.2	0.2	1	0.5	0.15	0.05
L7	70	90	0.2	0.15	1	−0.33	0.05	0.1
LV8	70	30	0.2	0.1	1	0	0.05	0.05
LV9	70	60	0.2	0.1	1	0	0.05	0.05
LV10	70	135	0.2	0.1	1	0	0.05	0.05
L11	30	90	0.1	0.1	1	0	0.05	0.05
L12	30	90	0.2	0.1	1	0	0.05	0.05
L13	30	90	0.3	0.1	1	0	0.05	0.05
L14	30	90	0.2	0.2	1	−0.5	0.05	0.15
L15	30	90	0.2	0.2	1	0	0.1	0.1
L16	30	90	0.2	0.2	1	0.5	0.15	0.05
LV17	30	30	0.2	0.1	1	0	0.05	0.05
LV18	30	60	0.2	0.1	1	0	0.05	0.05
LV19	30	135	0.2	0.1	1	0	0.05	0.05

Note: The label L stands for L-shaped loading with $\gamma = 90°$, while LV stands for $\gamma \neq 90°$ (non-orthogonal static and cyclic load directions).

Table 4
Numerical simulation programme for unidirectional loading cases.

Simulation label	Relative density D_r/%	ζ_b		ζ_c		ζ_{av}	ζ_{cyc}	$\zeta_{b,u}$	$\zeta_{c,u}$
		I	II	I	II				
U1	70	−0.1	0.2	1	0	0.1	0.1	0.1	−1
U2	70	0	0.1	1	0	0.05	0.05	0.1	0
U3	70	0	0.2	1	0	0.1	0.1	0.2	0
U4	70	0.1	0.1	1	0	0.05	0.05	0.2	0.5
U5	70	0.1	0.2	1	0	0.1	0.1	0.3	0.33
U6	70	0.2	0.1	1	0	0.05	0.05	0.3	0.67
U7	30	0	0.1	1	0	0.05	0.05	0.1	0
U8	30	0	0.2	1	0	0.1	0.1	0.2	0
U9	30	0.1	0.1	1	0	0.05	0.05	0.2	0.5
U10	30	0.1	0.2	1	0	0.1	0.1	0.3	0.33
U11	30	0.2	0.1	1	0	0.05	0.05	0.3	0.67

Note: The label U stands for unidirectional loading, i.e., with $\gamma = 0°$ in all cases.

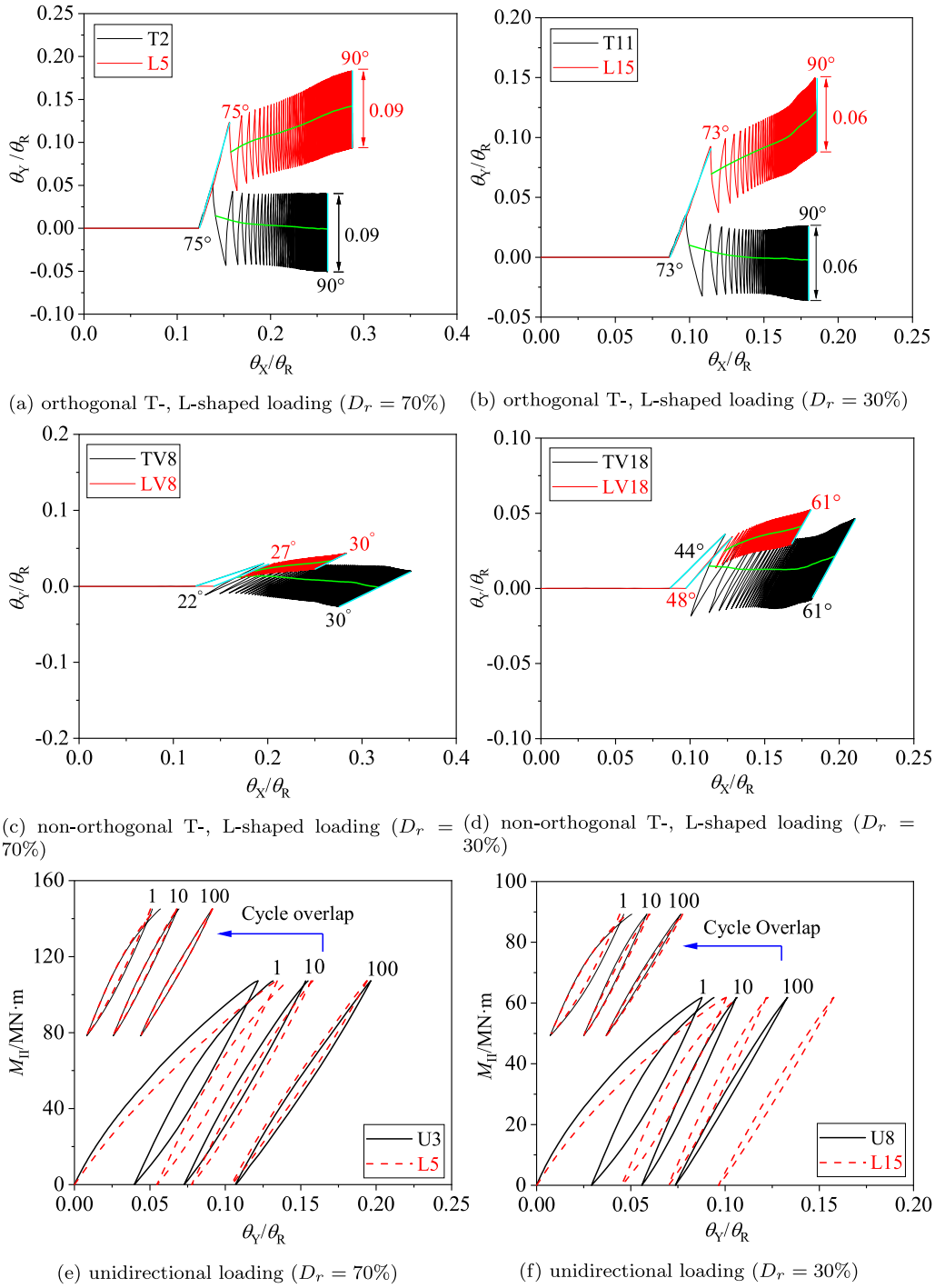

(a) orthogonal T-, L-shaped loading ($D_r = 70\%$)

(b) orthogonal T-, L-shaped loading ($D_r = 30\%$)

(c) non-orthogonal T-, L-shaped loading ($D_r = 70\%$)

(d) non-orthogonal T-, L-shaped loading ($D_r = 30\%$)

(e) unidirectional loading ($D_r = 70\%$)

(f) unidirectional loading ($D_r = 30\%$)

Fig. 5. Typical pile rotation responses to T- and L-shaped cyclic loading — both orthogonal ($\gamma = 90°$) and non-orthogonal ($\gamma \neq 90°$) – and comparison to unidirectional cyclic loading.

3.2. Cyclic soil mechanisms around the pile

This section explores how the cyclic ratcheting behaviour of the soil (as modelled via SANISAND-MS) scales up to determine the tilting response of the monopile under misaligned static–cyclic loading. To this end, the evolution under cycling of the stress state and the relative density in the soil around the pile are considered. In terms of nomenclature, the terminology illustrated in Fig. 8(a) is hereafter adopted: for a given direction of the static load M_{stat} (coinciding with the X axis), 'front' and 'back' pile sides are identified along the direction of M_{stat} to refer to soil zones under predominantly passive and active pressure conditions, respectively; along the perpendicular Y direction, 'left' and 'right' sides are defined relative to the direction of M_{stat}.

3.2.1. Cyclic stress evolution

To exemplify the evolution of soil stresses under T-shaped cyclic pile loading, all six independent components (i.e., σ_{xx}, σ_{yy}, σ_{zz}, τ_{xy}, τ_{yz}, τ_{zx} – subscripts are consistent with the coordinate system (x, y, z) in Fig. 1(a), and signs follow typical soil mechanics conventions) are plotted against the number of cycles n in Fig. 6 for the cases (a) T3 (in dense sand) and (b) T12 (in loose sand); in particular, the soil stresses associated with the reference element E1 in Fig. 1(b) are plotted, i.e., at

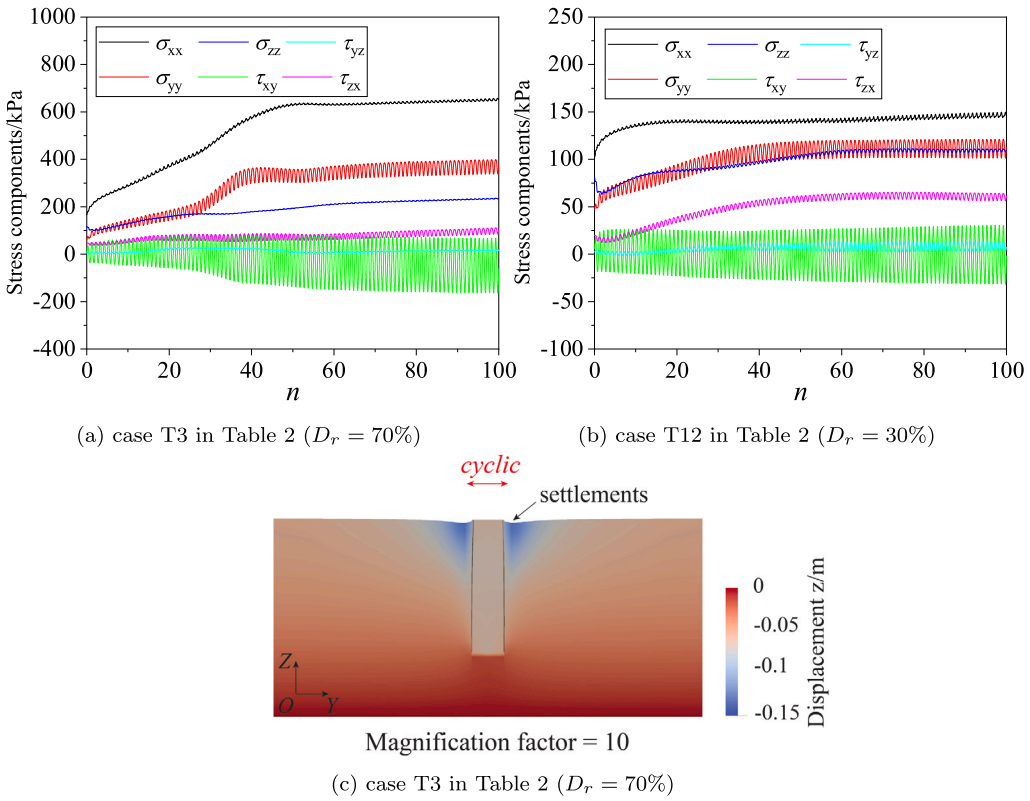

(a) case T3 in Table 2 ($D_r = 70\%$) (b) case T12 in Table 2 ($D_r = 30\%$)

(c) case T3 in Table 2 ($D_r = 70\%$)

Fig. 6. (a)–(b) Evolution of soil stress components under cyclic T-shaped loading at element E1 in Fig. 1(b); (c) example of final settlement distribution after T-shaped loading.

a location adjacent to the pile 4.5 m below the ground surface. Element E1 in the passive zone was selected to sample the soil response at a location where a large portion of the pile resistance to lateral loading is mobilised; in the case of L-shaped loading, element E2 on the left side (along the Y direction of pile deflection) is also considered.

Fig. 6 shows that, at a point in time immediately before cycling, the application of M_{stat} has already caused an increase of the horizontal stress σ_{xx} beyond the vertical component σ_{zz}, with a difference that is further magnified by the following 100 loading cycles. Among the tangential stress components, τ_{xy} most clearly reflects the application of the cyclic load according to a T-shaped path, while τ_{yz} and τ_{zx} experience only limited adjustments with minimal cyclic excursions, as a consequence of general equilibrium/compatibility conditions. The predominant cyclic variation of τ_{xy} emerges from the frictional interaction between the soil and pile surface under T-loading, in a fashion that is qualitatively similar in both dense (Fig. 6(a)) and loose (Fig. 6(b)) sands. The misaligned cyclic loading therefore has a twofold effect on the local response of the soil, in that it mobilises direct shearing along the direction of cycling, while enhancing the horizontal confining stress in the passive soil mass. Overall, the local behaviour of the soil at the considered location presents strong similarity with the response observed during drained cyclic DSS laboratory tests (Hsu and Vucetic, 2004). Similarly to cyclic DSS loading producing a compaction of the soil sample, T-shaped cycling induces visible compaction in the passive soil mass (Section 3.2.2) and soil settlement around the pile perimeter (Fig. 6(c)).

In order to describe the response to misaligned asymmetric cycling, Figs. 7(a)–7(b) presents similar cyclic stress information for case L3 in Table 3 (L-shaped loading in dense sand) at the two aforementioned elements E1 (passive side) and E2 (left side) – the corresponding results obtained for case T3 in Table 2 (T-shaped loading in dense sand) are reported in Figs. 7(c)–7(d) for comparison. While the soil in the passive zone (element E1) behaves in a broadly similar manner to what is observed in Fig. 6 (substantial permanent increase in σ_{xx} and cyclic τ_{xy} excursion), the largest cyclic stress variations in the reference left element (element E2) are associated with the stress components σ_{yy} and τ_{yz} – this is consistent with the response that one would expect under one-directional cyclic loading along the Y direction. Therefore, it may be concluded that L-shaped cycling is mainly resisted by soil mechanisms that may be termed, respectively, 'direct cyclic shearing' (in the passive zone) and 'cyclic compression' (in the side zones) – this terminology will continue to be used in the remainder of this paper. When comparing the evolution of all stress components in Figs. 7(a)–7(b) and 7(c)–7(d), it should be borne in mind that the T3 and L3 simulation cases share the same values of $\zeta_{b,I}$ and $\zeta_{b,II}$ (see Tables 2–3) with different resulting ζ_{cyc} (dimensionless cyclic loading excursion with respect to the average) – in the former case ($\zeta_{cyc}^{T3} = 0.1$) it is twice as big as in the latter case ($\zeta_{cyc}^{L3} = 0.05$). This difference stems directly from the different values set for the cyclic load asymmetry factor $\zeta_{c,II}$, which is necessary to obtain the target T- and L-shaped cyclic inputs. As a result, the cyclic variations of corresponding stress components are quantitatively rather different, with an impact, for instance, on the accumulated normalised rotation of the pile along the X direction (see Fig. 7(e)).

3.2.2. Cyclic relative density evolution

To complement the insight provided by Figs. 6–7, Fig. 8 shows the distribution of relative density at the soil surface after the static loading phase (Figs. 8(a)–8(b)) and the application of T-cycling (Figs. 8(c)–8(d)), both in dense (Figs. 8(a) and 8(c)) and loose (Figs. 8(b) and 8(d)) sands. As expected, the initial static loading produces a compressive densification in the passive zone, while dilation (due to compression relief) occurs in the active zone at the back of the pile, with no qualitative difference between piles in either dense or loose sand. Conversely, by the end of cyclic loading, more prominent densification and dilation have resulted at the front and back of the pile when in dense sand, whereas a net densification is found all around the pile in loose sand. Close inspection of stress paths in dense sand (not reported for brevity)

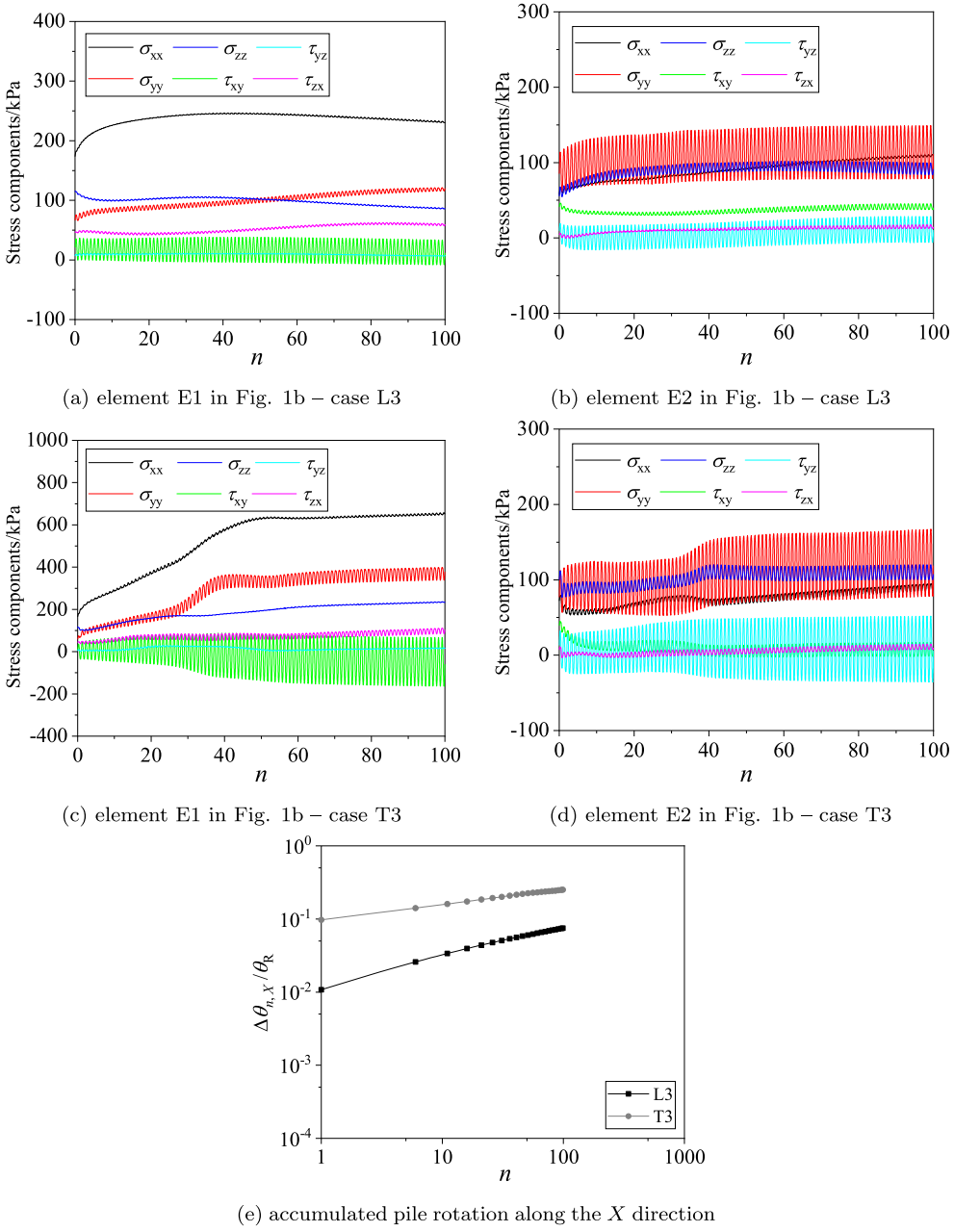

(a) element E1 in Fig. 1b – case L3

(b) element E2 in Fig. 1b – case L3

(c) element E1 in Fig. 1b – case T3

(d) element E2 in Fig. 1b – case T3

(e) accumulated pile rotation along the X direction

Fig. 7. Comparison between evolution of soil stress components under (a)–(b) L-shaped and (c)–(d) T-shaped cyclic loading in dense sand (D_r = 70%) – cases L3 in Table 3 vs. T3 in Table 2; (e) accumulated normalised pile rotation for L3 and T3 simulation cases.

has revealed that the phase transformation limit – i.e., transition from compactive to dilative behaviour (Li and Dafalias, 2000; Woo and Salgado, 2015) – is largely unattained in the passive zone in front of the pile, due to the relatively low amplitude of the applied cyclic load. This explains the strong similarities between the pile responses simulated in loose and dense sand.

Regarding the spatial extent of the densification zones, their limited size in the passive soil zone may be observed (where densification is mostly produced by the aforementioned – and relatively localised – direct cyclic shearing), while a much broader influence area (with a soil wedge as wide as approximately 90°) emerges on the left/right sides of the pile, i.e., along the Y direction of cycling. The latter occurrence is qualitatively similar to the densification patterns described by Liu et al. (2022a) for a monopile under one-directional loading.

For a more direct comparison, Fig. 9 reports the distribution of the relative density after unidirectional two-way loading (case U1 in Table 4) and its comparison to the corresponding results after T-shaped loading (case T2 in Table 2) – both cases relate to dense sand and the same fraction of cyclic load ($\zeta_{b,II}$ = 0.1, $\zeta_{c,II}$ = −1), although only T2 features preliminary static loading prior to (misaligned) cycling. As shown in Fig. 9(a), unidirectional symmetric cycling results in (superficial) soil densification all around the pile, with two obvious wedge-type zones that are most affected by the impact of repeated loading. In order to present densification patterns more clearly, iso-ΔD_r lines associated with ΔD_r = 1.5% and ΔD_r = 10% are shown in Fig. 9(b) for cases T2 and U1 – the soil inside the mentioned iso-ΔD_r lines has experienced the largest volumetric compaction. The static load appears to impact significantly the densification pattern at the back side of the pile, while it has little influence on the front and left/right sides. A possible reason for this occurrence is the limited overlap between the wedge-like influence zones associated with the static and cyclic compressive mechanisms: since the opening angles of the respective

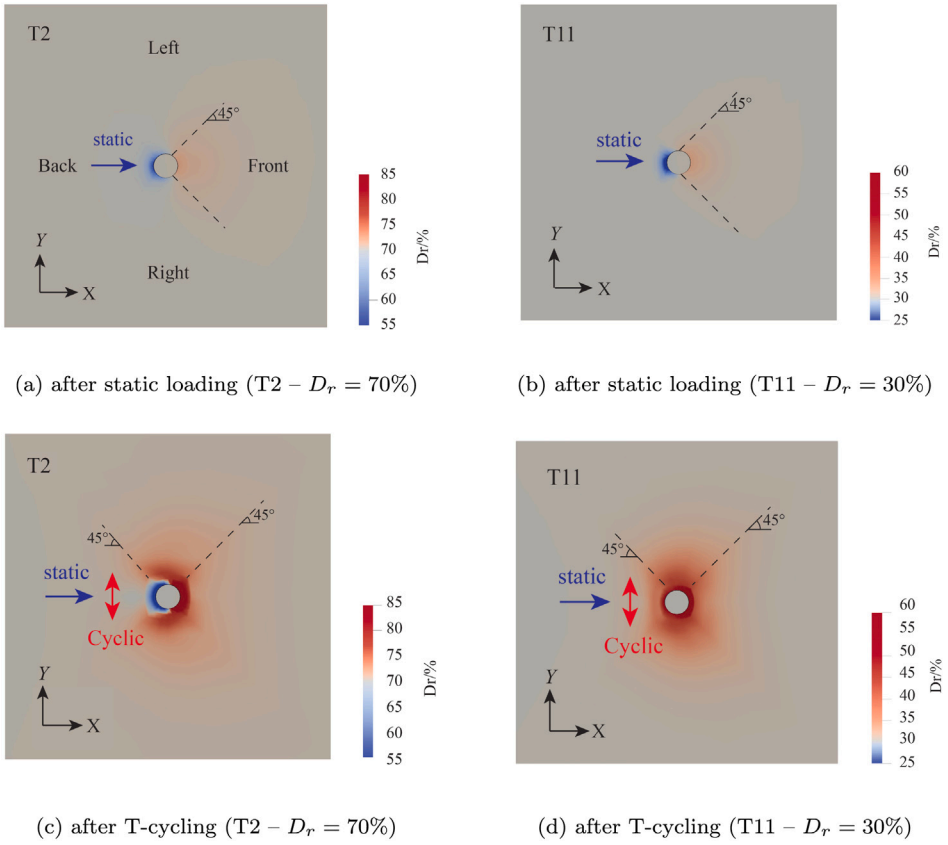

(a) after static loading (T2 – $D_r = 70\%$) (b) after static loading (T11 – $D_r = 30\%$)

(c) after T-cycling (T2 – $D_r = 70\%$) (d) after T-cycling (T11 – $D_r = 30\%$)

Fig. 8. Relative density distributions at soil surface for the cases T2 ($D_r = 70\%$) and T11 ($D_r = 30\%$) in Table 2, after static loading and 100 T-shaped loading cycles.

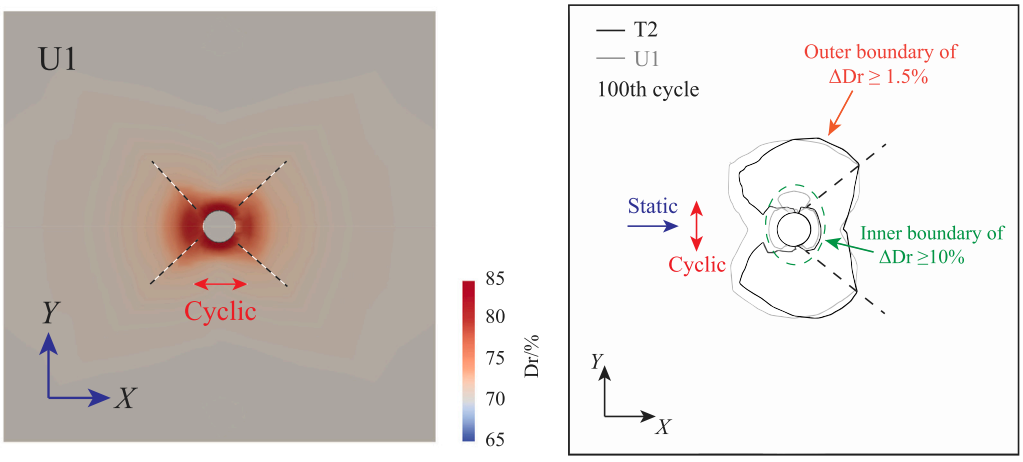

(a) Unidirectional loading (b) T-shaped vs unidirectional loading

Fig. 9. Comparison between superficial soil densification patterns after unidirectional two-way loading (case U1 in Table 4) and T-shaped loading (case T2 in Table 2) – initial $D_r = 70\%$.

wedges are limited in size, they do not 'constructively' interfere when $\gamma = 90°$ (wedge type), and therefore tend to generate densification patterns that are similar to those associated with unidirectional cycling only.

The influence of the cyclic loading direction on soil densification is further illustrated in Fig. 10, where the lines associated with a D_r increment of 1.5% are shown for L-shaped loading cases associated with four different load misalignment angles, namely $\gamma = 0°, 30°, 60°, 90°$ (respectively, cases U6, LV8, LV9, L2 in Tables 3–4) – all cases are for a pile in dense sand subjected to the same cyclic load amplitude but with different misalignment angle (γ). Overall, the four sub-figures clearly display the impact of γ, which causes a re-orientation of the ΔD_r contour lines as it is varied from 0° (wedge-type pattern) to 90° (flattened pattern). The obtained 3D FE results also support the belief that about 50 cycles are sufficient to attain the final configuration of the soil densification pattern (although the relative density per se may still continue to evolve to some extent).

The results reported in this section have shown monopile–soil interaction mechanisms that differ substantially from the case of pure unidirectional cyclic loading. In particular, the initial static load first compresses the soil in the passive zone, while the subsequent application of misaligned symmetric cycling (T-shaped loads) induces cyclic

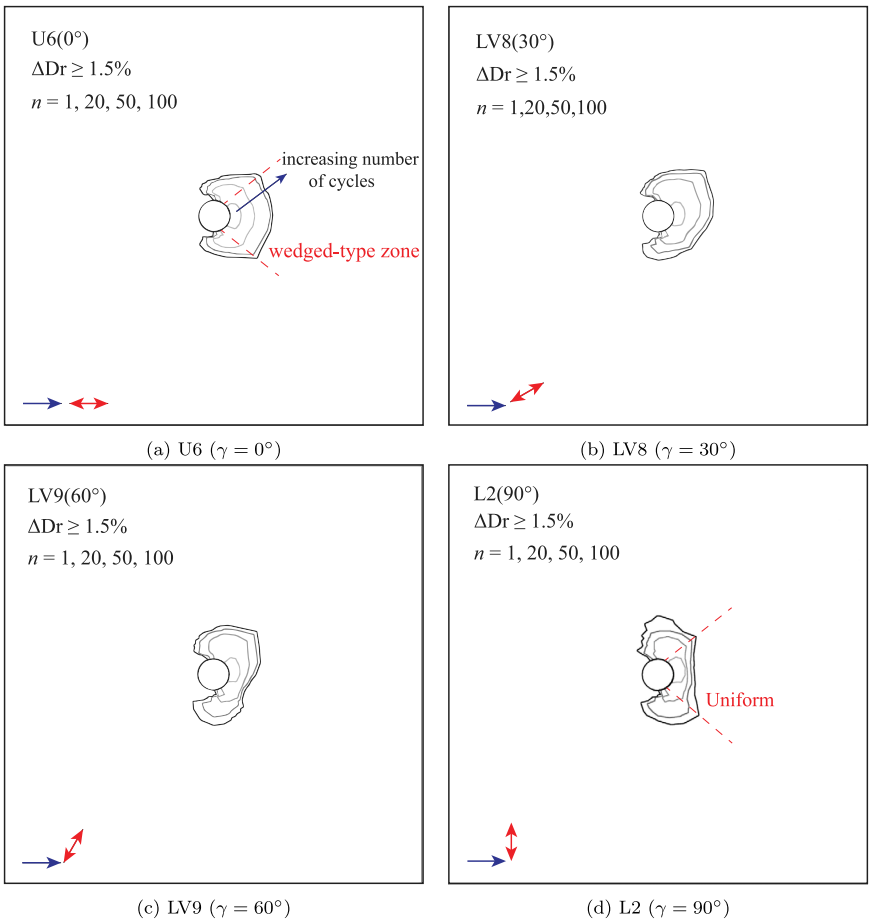

Fig. 10. Comparison among superficial soil densification patterns after L-shaped cycling with different load misalignment angles (cases U6, LV8, LV9, L2 in Tables 3–4) – initial $D_r = 70\%$.

shear stresses that produce further densification of the same zone; if asymmetric cyclic loading is applied (L-shaped loads), then the left zone also experiences compression — in a fashion that resembles the mechanism under unidirectional cyclic loading. Furthermore, when the static–cyclic load misalignment angle is changed, a clear relationship between this angle and the spatial orientation of the densification pattern is observed. The effects of these governing factors on cyclic tilt response of the pile are quantitatively analysed in the next section.

4. Parametric studies

After inspecting the main mechanisms of monopile–soil interaction under misaligned static–cyclic loads, the resulting tilt responses of the reference foundation (see Section 2) are discussed based on the results of detailed parametric analyses. The corresponding discussion is instrumental for quantifying the relevance of the main loading variables, and ultimately conceiving simplified approaches for cyclic pile tilt calculations.

4.1. Influence of $\zeta_{b,I}$ (static load magnitude) and $\zeta_{b,II} - \zeta_{c,II}$ (cyclic load magnitude and asymmetry)

Fig. 11 illustrates the influence of the static load magnitude on the cyclic accumulation of pile rotation. Under L-shaped loading (cases L1, L2, L3), increasing the magnitude of the static load ($\zeta_{b,I}$) is seen to enhance the total rotation induced by direct cyclic shearing (i.e., along the X direction), while it has negligible impact on the rotation caused by the cyclic compression mechanism in the orthogonal (i.e., Y) direction. In contrast, the influencing zone of the compressive loads is limited. This finding is consistent with Richards et al. (2020)'s experimental results, and is confirmed by the substantial agreement between the 'compressive' rotation increment $\Delta\theta_y$ and the corresponding trends for unidirectional loading of the same cyclic amplitude (cases U2 and U7 for dense and loose sand, respectively).

To explore the influence of the cyclic load amplitude (quantified by $\zeta_{b,II}$), the results of T-shaped simulations are compared in Fig. 12. The results indicate that, both in dense and loose sands, the larger the cyclic load amplitude, the more rotation that accumulates (along the X direction) as a consequence of the direct cyclic shear mechanism — which is therefore not directly comparable to pile ratcheting under unidirectional (compressive only) loading. The rotation accumulation trends in Fig. 12 appear to be mutually parallel for a given relative density, which implies a negligible influence of $\zeta_{b,II}$ on the ratcheting rate.

The cyclic asymmetry factor $\zeta_{c,II}$ determines the amplitude of the cyclic load excursion with respect to the corresponding average value after static loading. Decreasing $\zeta_{c,II}$ is in essence equivalent to increasing the intensity of the direct cyclic shear mechanism, which in turn enhances the accumulation of pile rotation along the X direction — see Fig. 13.

4.2. Influence of γ (static–cyclic load misalignment angle)

While the limited previous research has exclusively considered orthogonal T-shaped and L-shaped loads, the influence of static–cyclic load misalignment is explored herein by varying the misalignment angle γ. In the case of T-shaped loading, which is always cyclically symmetric (i.e., $\zeta_{c,II} = -1$), it is sufficient to account for γ values in

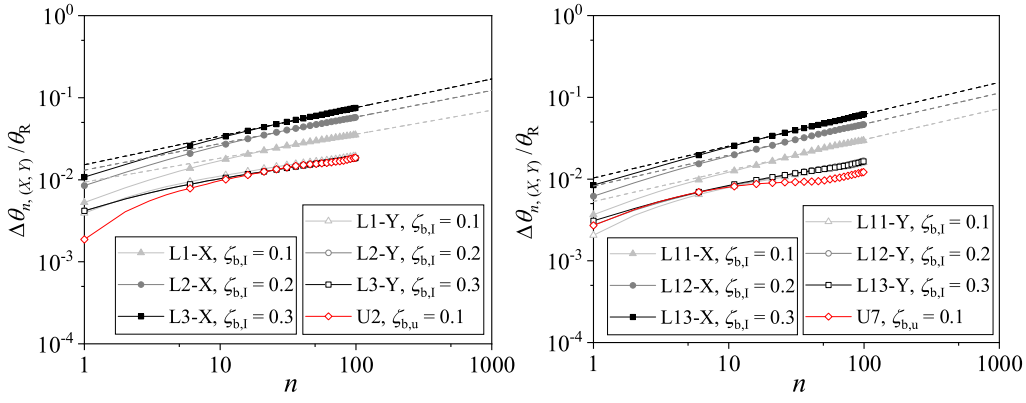

(a) $D_r = 70\%$ (b) $D_r = 30\%$

Fig. 11. Influence of the static load magnitude ($\zeta_{b,I}$) on the accumulated normalised pile rotation along the X and Y directions (L-shaped loading).

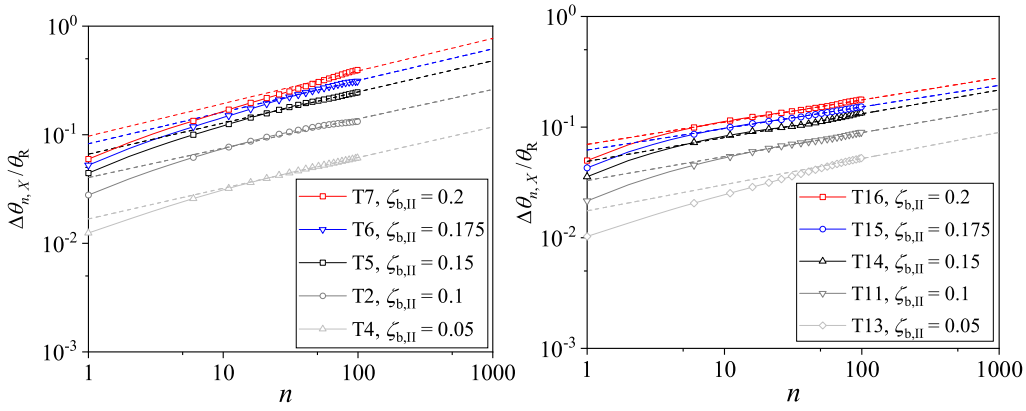

(a) $D_r = 70\%$ (b) $D_r = 30\%$

Fig. 12. Influence of the cyclic load magnitude ($\zeta_{b,II}$) on the accumulated normalised pile rotation along the X direction.

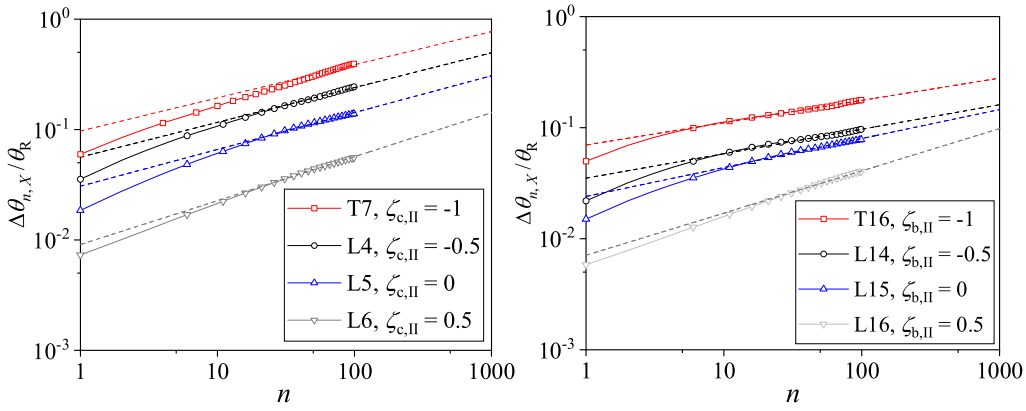

(a) $D_r = 70\%$ (b) $D_r = 30\%$

Fig. 13. Influence of the cyclic load asymmetry factor $\zeta_{c,II}$ on the accumulated normalised pile rotation along the X direction.

the range from 0° to 90°; conversely, L-shaped loading cases require γ to vary over 0°–180° for the whole range of possibilities to be covered. In general, unidirectional loading is retrieved when γ equals either 0° or 180°, but note that cycling occurs on opposite sides with respect to the intersection point O' in Fig. 2.

As is shown in Fig. 14, unidirectional load generates the largest accumulated pile rotation in comparison to orthogonal and non-orthogonal T-shaped cases — increasing γ values determine a gradual transition from compression- to shear-dominated pile tilt accumulation. Nevertheless, the differences obtained between the cases of, for instance, 0° and 30° or 60° and 90° are not substantial: in other words, the effects of non-orthogonal T-shaped loading may be approximately obtained by resorting to either unidirectional or orthogonal T-shaped cyclic loading — whichever is closest to the actual loading conditions. From a pile tilt standpoint, it seems as though the cyclic compressive mechanism is more 'damaging' than direct cyclic shearing, although

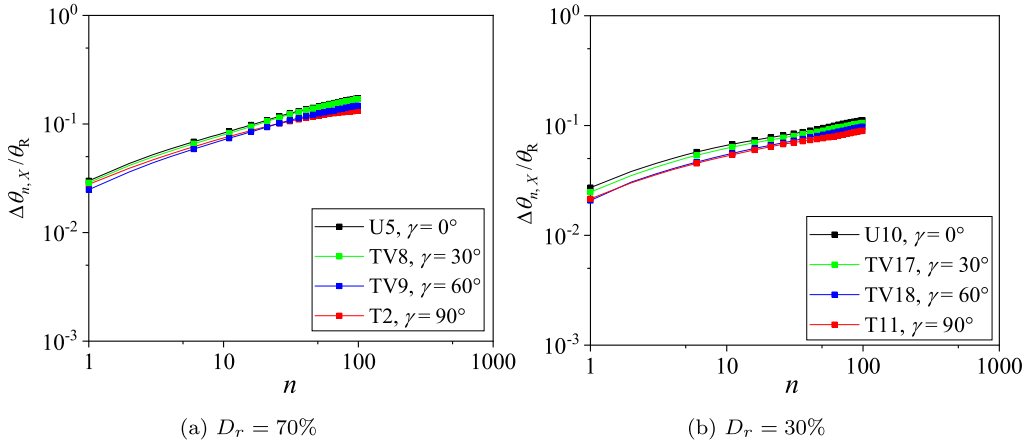

Fig. 14. Influence of the static–cyclic load misalignment angle γ on the accumulated normalised pile rotation along the X direction under T-shaped loading.

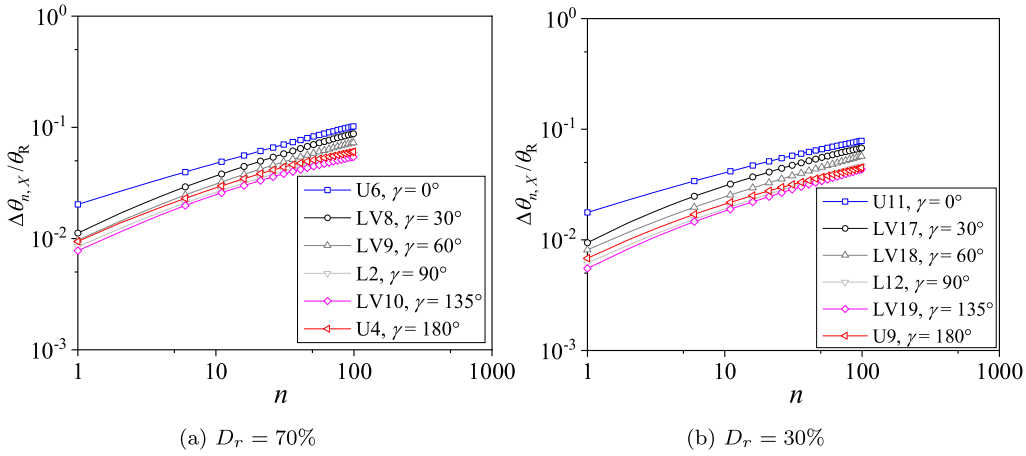

Fig. 15. Influence of the static–cyclic load misalignment angle γ on the accumulated normalised pile rotation along the X direction under L-shaped loading.

it is argued that the latter is likely to be substantially affected by the shear behaviour of the pile–soil interface.

Although L-shaped cycling can induce pile ratcheting along both the X and Y directions, only the former is considered in Fig. 15 to highlight the relationship between γ and the direct cyclic shear mechanism, and to facilitate the comparison with the T-shaped loading cases considered in Fig. 14. As already noted for T-shaped loading, the unidirectional loading case generates the largest deflection, almost twice the corresponding result under orthogonal L-shaped cycling. A gradual increase in γ tends to produce a reduction in pile ratcheting along the X direction (with the only exception being the $\gamma = 180°$ curve — see the above remark about the difference between $\gamma = 180°$ and $\gamma = 0°$).

4.3. Influence of ζ_{av} (average load during cycling)

To investigate the impact of the average load during cycling, simulation cases in which the cyclic load amplitude factor ζ_{cyc} is set to 0.1 are considered, while ζ_{av} varies between 0 and 0.1. In fact, varying ζ_{av} is equivalent to studying how the 'eccentricity' of the cyclic mean load (with respect to the static load) influences the pile ratcheting behaviour. As shown in Fig. 16, such an influence becomes close to negligible as the number of loading cycles increases — at least, within the first 100 cycles considered herein.

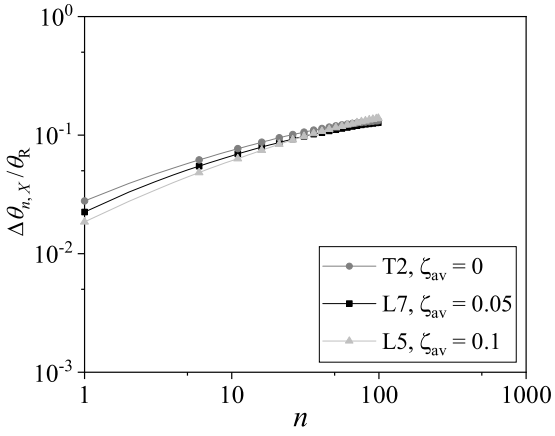

Fig. 16. Influence of average load during cycling ζ_{av} on the accumulated normalised pile rotation along the X direction – $D_r = 70\%$.

5. An empirical law for monopile tilt induced by cyclic shearing

The pile deflection induced by T- or L-shaped cyclic loading cannot be straightforwardly reproduced by existing empirical pile tilting laws,

such as that proposed, for instance, by LeBlanc et al. (2010a) (Eq. (1)). To overcome this limitation, a new version of Eq. (1) that is applicable to the cyclic shearing mechanism described above (i.e., for orthogonal static and cyclic loads) is proposed hereafter in light of the presented 3D FE results.

5.1. Formulation and calibration

Building on LeBlanc et al.'s formulation, a similar power-law relationship between the accumulated pile rotation $\Delta\theta_{n,X}$ (along the direction of the static load) and the number of cycles n is preserved, which has turned out to remain suitable for fitting the above pile ratcheting trends in the presence of static–cyclic load misalignment — see Figs. 11–13, where the dashed lines are the result of curve-fitting the 3D FE results using the following equation:

$$\frac{\Delta\theta_{n,X}}{\theta_R} = A \cdot n^B \tag{10}$$

In Eq. (10), the parameters A and B were identified through a curve-fitting procedure (either numerical or experimental results may generally be used to this end). The 3D FE results discussed in this study indicate that the main governing load factors include the magnitude of the static load, as well as the magnitude and asymmetry of the cyclic load component; the quantitative influence of the sand relative density has been underlined as well. Based on these premises, Eq. (10) is further specified to determine the accumulated normalised rotation $\Delta\theta_{n,X}$ under orthogonal cyclic shearing:

$$\frac{\Delta\theta_{n,X}}{\theta_R} = T^{cs}_{b,I}(\zeta_{b,I}, D_r)\cdot T^{cs}_{b,II}(\zeta_{b,II}, D_r)\cdot T^{cs}_{c,II}(\zeta_{c,II})\cdot n^{\alpha(\zeta_{c,II}, D_r)} \tag{11}$$

where $A = T^{cs}_{b,I}(\zeta_{b,I}, D_r)\cdot T^{cs}_{b,II}(\zeta_{b,II}, D_r)\cdot T^{cs}_{c,II}(\zeta_{c,II})$ and $B = \alpha(\zeta_{c,II}, D_r)$ – cf. to Eq. (10). In order to separately identify the three functions $T^{cs}_{b,I}$, $T^{cs}_{b,II}$, and $T^{cs}_{c,II}$, the assumptions $T^{cs}_{b,II}(\zeta_{b,II} = 0.1) = 1$ and $T^{cs}_{c,II}(\zeta_{c,II} = -1) = 1$ are introduced as pivotal settings — such settings play the same role as the assumption $T_c\left(\zeta_c = 0\right) = 1$ in Eq. (1) (LeBlanc et al., 2010a). It should be noted that the superscript *cs* in Eq. (11) refers explicitly to the cyclic shearing mechanism, for distinction from the complementary compressive mechanism that dominates unidirectional loading cases (and for which Eq. (1) was originally conceived). Based on these two assumptions, numerical results associated with a varying $\zeta_{b,I}$ were first considered to derive $T_{b,I}$; then, the parametric studies on the influence of $\zeta_{b,II}$ and $\zeta_{c,II}$ enabled the identification of the other two functions, $T_{b,II}$ and $T_{c,II}$. The normalisation with respect to θ_R on the left-hand side is typically introduced to account for pile size effects, although extending the use of the same calibrated functions to different pile geometries would require additional numerical and/or experimental analyses.

In contrast with LeBlanc et al.'s proposal, the results obtained in this study confirm the dependence of the ratcheting exponent α on the cyclic asymmetry factor $\zeta_{c,II}$ and the relative density D_r, which is in line with the more recent experimental findings, for instance, of (Truong et al., 2019). This fact is supported by Figs. 11–13, and summarised in Fig. 17, where an approximately linear dependence of α on $\zeta_{c,II}$ is shown for both considered D_r values.

As shown in Fig. 18, the three functions $T^{cs}_{b,I}$, $T^{cs}_{b,II}$, and $T^{cs}_{c,II}$ have been identified against 3D FE results. Figs. 18(a) and 18(b) display the approximately linear relationship between the amplitude of the static ($\zeta_{b,I}$) and cyclic ($\zeta_{b,II}$) load components and, respectively, the $T^{cs}_{b,I}$ and $T^{cs}_{b,II}$ functions, with significant impact of the relative density; conversely, the relative density seems to have no influence on the third function $T^{cs}_{c,II}$. These features of the functions $T^{cs}_{b,I}$, $T^{cs}_{b,II}$, and $T^{cs}_{c,II}$ are very consistent with previous findings regarding unidirectional cyclic loading conditions (LeBlanc et al., 2010a).

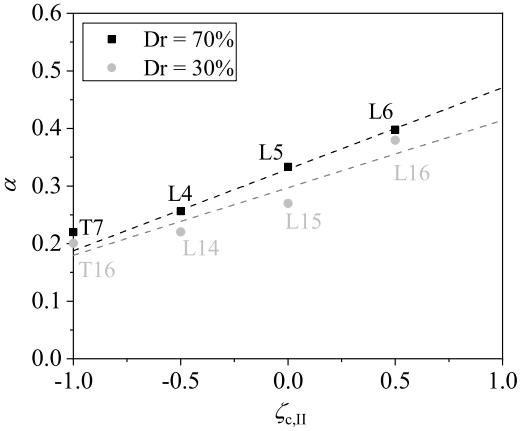

Fig. 17. Influence of $\zeta_{c,II}$ on the ratcheting exponent α in Eq. (11) for dense and loose sand.

5.2. A calculation example

The general case in which a cyclic loading component F is misaligned with respect to the static load (oriented along the X direction) may be tackled by decomposing F into its orthogonal cyclic components F_X and F_Y. Accordingly, F_Y is orthogonal to the static load and may be regarded as responsible for pile rotation accumulation along the X direction through the aforementioned cyclic shear mechanism; conversely, F_X is aligned with the static load and causes X-tilt accumulation through the cyclic compression mechanism. Both F_X and F_Y can individually induce cyclic accumulation of the pile deflection, which can be separately estimated by using the respective empirical equations – Eqs. (1) and (11) – with the associated values of the relevant dimensionless load factors. In the case of F_X and F_Y acting simultaneously, it would a priori be uncertain how their individual effects could be combined to obtain the combined response of the pile to misaligned static–cyclic loading. Fig. 19 provides some insight into how such a combination could be performed for four different 3D FE simulation cases (LV8, LV17, LV9, LV18 — black lines), not previously adopted for the calibration of the $T^{cs}_{b,I}$, $T^{cs}_{b,II}$ and $T^{cs}_{c,II}$ functions in Eq. (11). In Fig. 19:

- the blue and red curves indicate the X-tilt of the pile individually produced by F_X (cyclic compressive mechanism) and F_Y (cyclic shear mechanism) – results obtained by means of additional 3D FE simulations;
- the grey line represents the superposition by direct summation of the individual rotation contributions, while the magenta line is obtained as the square root of the sum of the squares (SRSS);
- the cyan circular markers are associated with the combination method proposed by Lin and Liao (1999), based on the application of so-called Miner's rule[1].

The four examples illustrated in the figure support that conjecture that the SRSS approach is the most suitable for estimating cyclic pile rotation under misaligned static–cyclic loading. Possible reasons for the superior performance of the SRSS include (i) the relatively fast evolution of cyclic stress paths in the soil towards nearly steady conditions, and (ii) the limited magnitude of the considered cyclic loads with respect to lateral pile capacity (which is intrinsic to realistic operational loading conditions).

[1] The Miner's rule-based superposition method was proposed for calculating soil strain or pile deflection under cyclic load parcels of different amplitude. The equivalent cycle number between two consecutive cyclic loads can be calculated based on the same amount of strain or deflection. The equivalent cycle number will be added into the next load parcel.

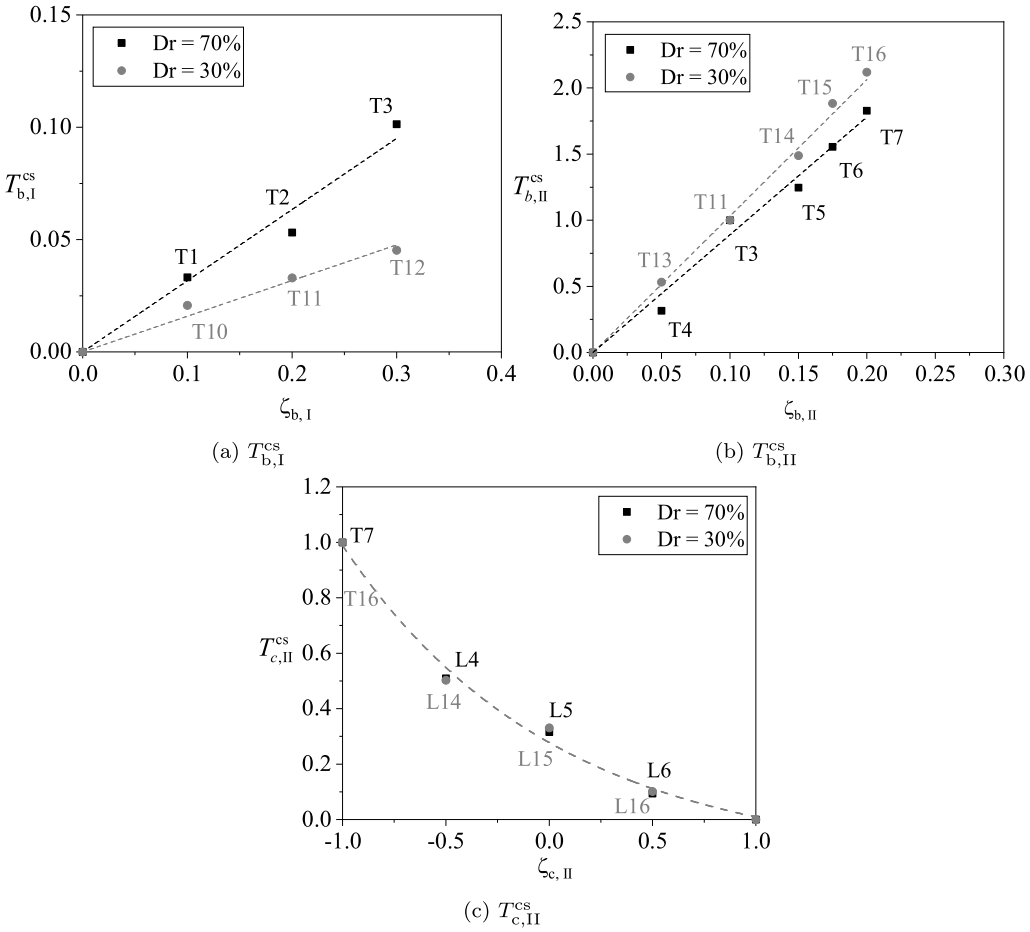

Fig. 18. Dependence of the functions $T^{cs}_{b,I}$, $T^{cs}_{b,II}$, and $T^{cs}_{c,II}$ in Eq. (11) on the dimensionless load factors $\zeta_{b,I}$, $\zeta_{b,II}$, and $\zeta_{c,II}$.

6. Concluding remarks

Offshore wind turbines are subjected in reality to repeated wind and wave loads of random magnitude and direction. In an effort to explore essential features of offshore soil–foundation interaction for the case of monopiles, this paper has presented a numerical investigation on the influence of the misalignment between wind (nearly static) and wave loads (prominently cyclic) on the cyclic accumulation of monopile rotation. Emphasis has been on gaining insight into, and proposing a simplified prediction method for, the response of offshore monopiles to more complex/realistic loading conditions than usually considered (i.e., with no load misalignment). To simplify the definition of a meaningful numerical simulation programme, the reference cases of T-shaped and L-shaped loading have been introduced to distinguish the cases in which cycling either is or is not applied symmetrically around the initial static load; furthermore, the effects of the load magnitude and symmetry as well as the load misalignment degree have been investigated quantitatively.

The established 3D FE simulation programme has been carried out by considering a single monopile (with a 5 m diameter and embedded length of 20 m) in Karlsruhe quartz sand — the SANISAND-MS model, previously calibrated for this sand, has been used throughout the study to reproduce its behaviour under loose (D_r = 30%) and dense (D_r = 70%) conditions. The whole set of numerical results have led to the following conclusions:

(a) T-shaped loading can produce non-negligible accumulation of pile tilt with decreasing rate (ratcheting) along the direction of the static load, while L-shaped loading can produce cyclic tilt accumulation along both the static and cyclic directions due to the asymmetry of its cyclic part. This asymmetry is more damaging for the pile rotation along the static loading direction;

(b) the soil mechanisms underlying the pile ratcheting response along the static loading direction are fundamentally different under either T/L-cycling or unidirectional loading in terms of the associated evolution of the stress state and soil density around the pile. In the former case, a prominent direct shearing effect is present (when the cyclic loading is symmetric), and this will co-exist with a cyclic compressive mechanism (when the cyclic loading is asymmetric), which is the sole relevant mechanism under unidirectional loading;

(c) the cyclic compression mechanism tends to be more damaging rotation-wise than a direct shear cycling of equal amplitude. When the cyclic load deviates from the static load gradually, the pile response will be increasingly affected by the latter mechanism;

(d) T/L-shaped loading is defined by three elements — namely, static load magnitude, cyclic load magnitude, and cyclic (a) symmetry. Based on detailed parametric studies, a new empirical equation suitable for cyclic-shear dominated loading (perpendicular T/L-shaped loading) is proposed. The corresponding $T^{cs}_{b,I}$ and $T^{cs}_{b,II}$ functions have been found to linearly depend on the load magnitude (static and cyclic, respectively), while $T^{cs}_{c,II}$ does not seem to be influenced by the relative density of the soil. These findings are consistent with previous work on unidirectional cyclic loading, and can be adopted as sound working assumptions in future applications of the proposed framework to design practice;

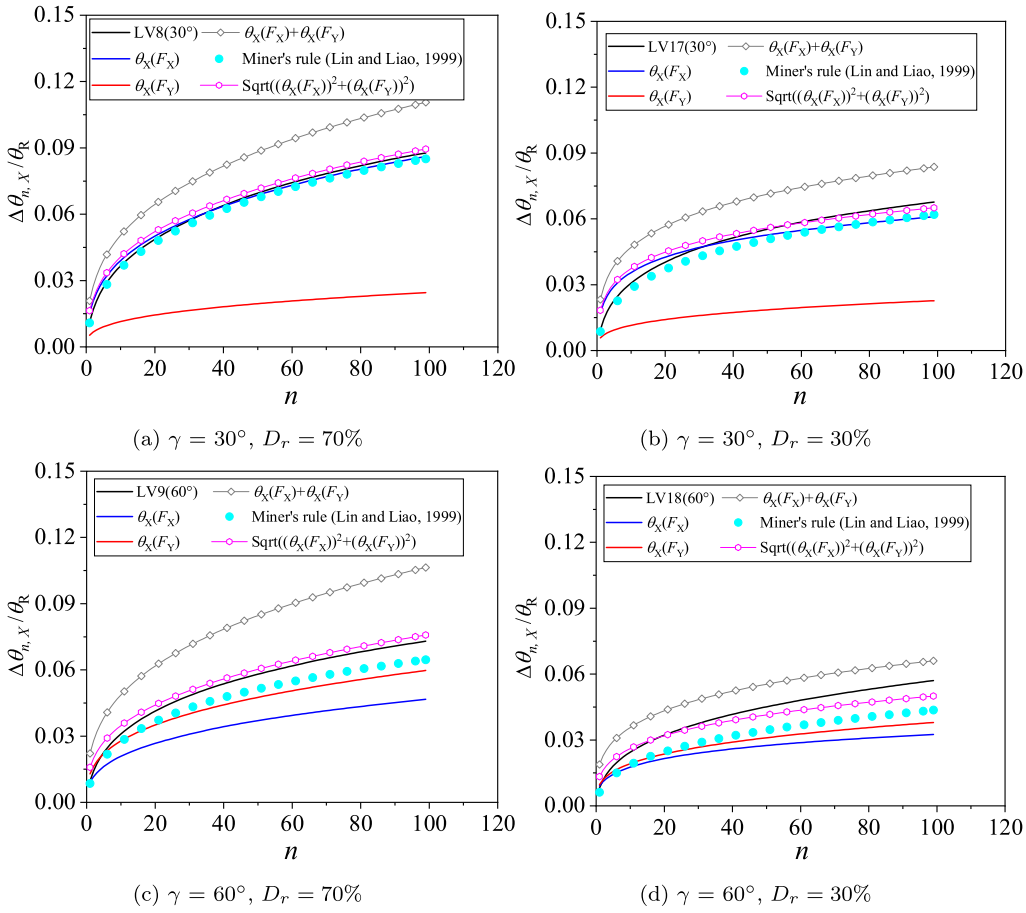

Fig. 19. Prediction of the pile ratcheting behaviour under non-orthogonal L-shaped loading.

(e) in the case of non-orthogonal T/L-shaped loading, decomposing the cyclic load into two orthogonal components, calculating their respective pile accumulated rotation and, lastly, combining them based on the square-root-of-the-sum-of-the-squares (SRSS) method can provide accurate estimates of cyclic pile tilt as obtained via more detailed 3D FE analyses.

The findings and calculation framework proposed in this study represent what is believed to be a valuable addition to the growing body of knowledge regarding cyclically loaded monopiles. Utilisation in geotechnical design practice will require further computational and experimental studies to confirm the extension of the presented results to different soils and monopile geometries, as well as their extrapolation to longer cyclic loading histories.

CRediT authorship contribution statement

Zheng Li: Conceptualization, Methodology, Software, Validation, Formal analysis, Data curation, Writing – original draft. **Haoyuan Liu:** Methodology, Software, Writing – review & editing. **Michael A. Hicks:** Funding acquisition, Supervision, Writing – review & editing. **Federico Pisanò:** Funding acquisition, Conceptualization, Methodology, Supervision, Writing – original draft.

Declaration of competing interest

The authors declare that they have no known competing financial interests or personal relationships that could have appeared to influence the work reported in this paper.

Data availability

Data will be made available on request.

Acknowledgements

The authors wish to acknowledge the China Scholarship Council (CSC) and the Geo-Engineering Section of Delft University of Technology, China for financial support of the first author.

References

Achmus, M., Kuo, Y.-S., Abdel-Rahman, K., 2009. Behavior of monopile foundations under cyclic lateral load. Comput. Geotech. 36 (5), 725–735.
Albiker, J., Achmus, M., Frick, D., Flindt, F., 2017. 1 g model tests on the displacement accumulation of large-diameter piles under cyclic lateral loading. Geotech. Test. J. 40 (2), 173–184.
API, 2011. Geotechnical and foundation design considerations.
Arany, L., Bhattacharya, S., Macdonald, J., Hogan, S., 2017. Design of monopiles for offshore wind turbines in 10 steps. Soil Dyn. Earthq. Eng. 92, 126–152.
Byrne, B.W., Burd, H.J., Zdravkovic, L., Abadie, C.N., Houlsby, G.T., Jardine, R.J., Martin, C.M., McAdam, R.A., Pacheco Andrade, M., Pedro, A.M., et al., 2019. PISA design methods for offshore wind turbine monopiles. In: Offshore Technology Conference. Offshore Technology Conference.
Cheng, X., Diambra, A., Ibraim, E., Liu, H.Y., Pisanò, F., 2021. 3D FE-informed laboratory soil testing for the design of offshore wind turbine monopiles. J. Mar. Sci. Eng. 9 (1), 101.
Corciulo, S., Zanoli, O., Pisanò, F., 2017. Transient response of offshore wind turbines on monopiles in sand: role of cyclic hydro–mechanical soil behaviour. Comput. Geotech. 83, 221–238.
Corti, R., Diambra, A., Muir Wood, D., Escribano, D.E., Nash, D.F., 2016. Memory surface hardening model for granular soils under repeated loading conditions. J. Eng. Mech. 04016102.
Dafalias, Y.F., Manzari, M.T., 2004. Simple plasticity sand model accounting for fabric change effects. J. Eng. Mech. 130 (6), 622–634.

DNV, G., 2016. DNVGL-ST-0126: Support Structures for Wind Turbines. DNV GL, Oslo, Norway.
Dührkop, J., Grabe, J., 2008. Monopilegründungen von offshore-windenergieanlagen–zum einfluss einer veränderlichen zyklischen lastangriffsrichtung. Bautechnik 85 (5), 317–321.
Frick, D., Achmus, M., 2020. An experimental study on the parameters affecting the cyclic lateral response of monopiles for offshore wind turbines in sand. Soils Found. 60 (6), 1570–1587.
Ghofrani, A., Arduino, P., 2018. Prediction of LEAP centrifuge test results using a pressure-dependent bounding surface constitutive model. Soil Dyn. Earthq. Eng. 113, 758–770.
Griffiths, D.V., 1985. Numerical modelling of interfaces using conventional finite elements. In: Fifth International Conference on Numerical Methods in Geomechanics. Nagoya, pp. 837–844.
Hsu, C.-C., Vucetic, M., 2004. Volumetric threshold shear strain for cyclic settlement. J. Geotech. Geoenviron. Eng. 130 (1), 58–70.
Jenck, O., Obaei, A., Emeriault, F., Dano, C., 2021. Effect of horizontal multidirectional cyclic loading on piles in sand: A numerical analysis. J. Mar. Sci. Eng. 9 (2), 235.
Kaggwa, W.S., Booker, J.R., Carter, J., 1991. Residual strains in calcareous sand due to irregular cyclic loading. J. Geotech. Eng. 117 (2), 201–218.
Kaynia, A.M., 2021. Analysis of Pile Foundations Subject to Static and Dynamic Loading. CRC Press.
Kementzetzidis, E., Corciulo, S., Versteijlen, W.G., Pisanò, F., 2019. Geotechnical aspects of offshore wind turbine dynamics from 3D non-linear soil-structure simulations. Soil Dyn. Earthq. Eng. 120, 181–199.
Klinkvort, R.T., Hededal, O., 2013. Lateral response of monopile supporting an offshore wind turbine. Proc. Inst. Civ. Eng.-Geotech. Eng. 166 (2), 147–158.
Leblanc, C., Byrne, B., Houlsby, G., 2010b. Response of stiff piles to random two-way lateral loading. Géotechnique 60 (9), 715–721.
LeBlanc, C., Houlsby, G., Byrne, B., 2010a. Response of stiff piles in sand to long-term cyclic lateral loading. Géotechnique 60 (2), 79–90.
Li, X.S., Dafalias, Y.F., 2000. Dilatancy for cohesionless soils. Géotechnique 50 (4), 449–460.
Li, W., Igoe, D., Gavin, K., 2015. Field tests to investigate the cyclic response of monopiles in sand. Proc. Inst. Civ. Eng.-Geotech. Eng. 168 (5), 407–421.
Lin, S.-S., Liao, J.-C., 1999. Permanent strains of piles in sand due to cyclic lateral loads. J. Geotech. Geoenviron. Eng. 125 (9), 798–802.
Liu, H.Y., Abell, J.A., Diambra, A., Pisanò, F., 2019. Modelling the cyclic ratcheting of sands through memory-enhanced bounding surface plasticity. Géotechnique 69 (9), 783–800.
Liu, H.Y., Diambra, A., Abell, J.A., Pisanò, F., 2020. Memory-enhanced plasticity modeling of sand behavior under undrained cyclic loading. J. Geotech. Geoenviron. Eng. 146 (11), 04020122.
Liu, H.Y., Kaynia, A.M., 2021. Characteristics of cyclic undrained model SANISAND-MSu and their effects on response of monopiles for offshore wind structures. Géotechnique 1–39.
Liu, H., Kementzetzidis, E., Abell, J.A., Pisanò, F., 2022a. From cyclic sand ratcheting to tilt accumulation of offshore monopiles: 3D FE modelling using SANISAND-MS. Géotechnique 72 (9), 753–768.
Liu, H.Y., Pisanò, F., 2019. Prediction of oedometer terminal densities through a memory-enhanced cyclic model for sand. Géotech. Lett. 9 (2), 81–88. http://dx.doi.org/10.1680/jgele.18.00187.
Liu, H., Pisanò, F., Jostad, H.P., Sivasithamparam, N., 2022b. Impact of cyclic strain accumulation on the tilting behaviour of monopiles in sand: An assessment of the Miner's rule based on SANISAND-MS 3D FE modelling. Ocean Eng. 250, 110579.
Liu, H.Y., Zygounas, F., Diambra, A., Pisanò, F., 2018. Enhanced plasticity modelling of high-cyclic ratcheting and pore pressure accumulation in sands. In: Numerical Methods in Geotechnical Engineering IX: Proceedings of the 9th European Conference on Numerical Methods in Geotechnical Engineering (NUMGE 2018), June 25-27, 2018. CRC Press, Porto, Portugal, p. 87.
Lovera, A., Ghabezloo, S., Sulem, J., Randolph, M.F., Kham, M., Palix, E., 2021. Pile response to multi-directional lateral loading using P–y curves approach. Géotechnique 71 (4), 288–298.
Lovera, A., S. Ghabezloo, J.S., Randolph, M.F., Kham, M., Palix, E., 2019. Effects of a multi-directional loading sequence on offshore wind turbine natural frequencies. In: Proceedings of the XVII ECSMGE-2019, Vol. 168. Thomas Telford Ltd, pp. 407–421.
McGann, C.R., Arduino, P., Mackenzie-Helnwein, P., 2015. A stabilized single-point finite element formulation for three-dimensional dynamic analysis of saturated soils. Comput. Geotech. 66, 126–141.
McKenna, F., 2011. OpenSees: a framework for earthquake engineering simulation. Comput. Sci. Eng. 13 (4), 58–66.
Nanda, S., Arthur, I., Sivakumar, V., Donohue, S., Bradshaw, A., Keltai, R., Gavin, K., Mackinnon, P., Rankin, B., Glynn, D., 2017. Monopiles subjected to uni-and multi-lateral cyclic loading. Proc. Inst. Civ. Eng.-Geotech. Eng. 170 (3), 246–258.
Niemunis, A., Wichtmann, T., Triantafyllidis, T., 2005. A high-cycle accumulation model for sand. Comput. Geotech. 32 (4), 245–263.
Page, A.M., Grimstad, G., Eiksund, G.R., Jostad, H.P., 2019. A macro-element model for multidirectional cyclic lateral loading of monopiles in clay. Comput. Geotech. 106, 314–326.
Page, A.M., Klinkvort, R.T., Bayton, S., Zhang, Y., Jostad, H.P., 2021. A procedure for predicting the permanent rotation of monopiles in sand supporting offshore wind turbines. Mar. Struct. 75, 102813.
Peralta, P., 2010. Investigations on the Behavior of Large Diameter Piles under Long-Term Lateral Cyclic Loading in Cohesionless Soil. na.
Pisanò, F., 2019. Input of advanced geotechnical modelling to the design of offshore wind turbine foundations. In: Proceedings of the 17th European Conference on Soil Mechanics and Geotechnical Engineering (ECSMGE 2019). International Society of Soil Mechanics and Geotechnical Engineering.
Ramírez, L., Fraile, D., Brindley, G., 2020. Offshore Wind in Europe: Key Trends and Statistics 2020. Technical report.
Richards, I., 2019. Monopile Foundations under Complex Cyclic Lateral Loading (Ph.D. thesis). University of Oxford.
Richards, I., Bransby, M., Byrne, B., Gaudin, C., Houlsby, G., 2021. Effect of stress level on response of model monopile to cyclic lateral loading in sand. J. Geotech. Geoenviron. Eng. 147 (3), 04021002.
Richards, I.A., Byrne, B.W., Houlsby, G.T., 2020. Monopile rotation under complex cyclic lateral loading in sand. Géotechnique 70 (10), 916–930.
Rudolph, C., Bienen, B., Grabe, J., 2014. Effect of variation of the loading direction on the displacement accumulation of large-diameter piles under cyclic lateral loading in sand. Can. Geotech. J. 51 (10), 1196–1206.
Scott, M.H., Fenves, G.L., 2003. A Krylov subspace accelerated Newton algorithm. In: 2003 ASCE/SEI Structures Congress and Exposition: Engineering Smarter.
Sheil, B.B., McCabe, B.A., 2017. Biaxial loading of offshore monopiles: numerical modeling. Int. J. Geomech. 17 (2), 04016050.
Sloan, S.W., 1987. Substepping schemes for the numerical integration of elastoplastic stress–strain relations. Internat. J. Numer. Methods Engrg. 24 (5), 893–911.
Truong, P., Lehane, B., Zania, V., Klinkvort, R.T., 2019. Empirical approach based on centrifuge testing for cyclic deformations of laterally loaded piles in sand. Géotechnique 69 (2), 133–145.
Wichtmann, T., 2005. Explicit Accumulation Model for Non-Cohesive Soils under Cyclic Loading (Ph.D. thesis). Inst. für Grundbau und Bodenmechanik Braunschweig, Germany.
Woo, S.I., Salgado, R., 2015. Bounding surface modeling of sand with consideration of fabric and its evolution during monotonic shearing. Int. J. Solids Struct. 63, 277–288.
Zhao, L., Bransby, M., Gaudin, C., 2020. Centrifuge observations on multidirectional loading of a suction caisson in dense sand. Acta Geotech. 15 (6), 1439–1451.
Zhu, F., Bienen, B., O'Loughlin, C., Morgan, N., Cassidy, M.J., 2018. The response of suction caissons to multidirectional lateral cyclic loading in sand over clay. Ocean Eng. 170, 43–54.